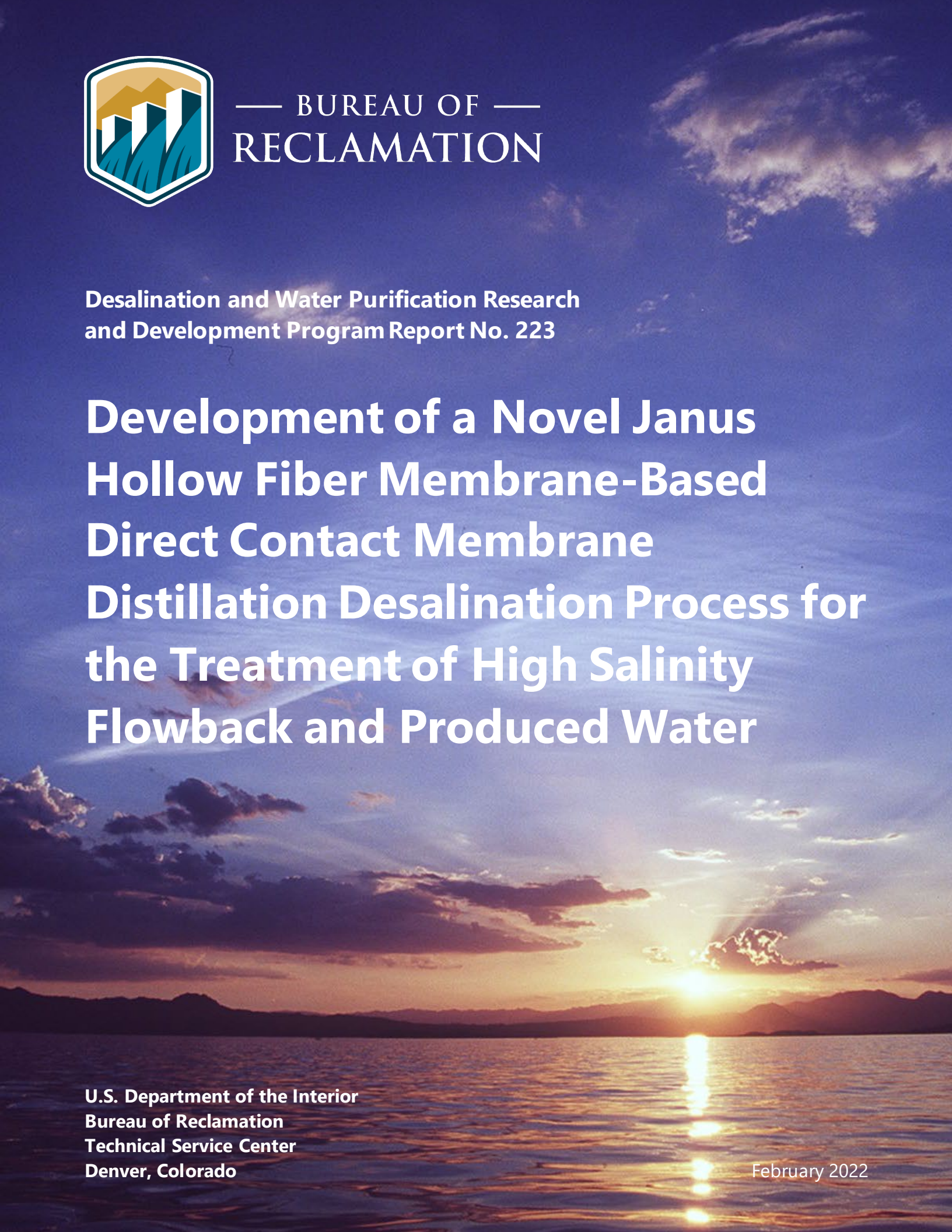

BUREAU OF RECLAMATION

Desalination and Water Purification Research and Development Program Report No. 223

Development of a Novel Janus Hollow Fiber Membrane-Based Direct Contact Membrane Distillation Desalination Process for the Treatment of High Salinity Flowback and Produced Water

U.S. Department of the Interior
Bureau of Reclamation
Technical Service Center
Denver, Colorado

February 2022

REPORT DOCUMENTATION PAGE

Form Approved
OMB No. 0704-0188

The public reporting burden for this collection of information is estimated to average 1 hour per response, including the time for reviewing instructions, searching existing data sources, gathering and maintaining the data needed, and completing and reviewing the collection of information. Send comments regarding this burden estimate or any other aspect of this collection of information, including suggestions for reducing the burden, to Department of Defense, Washington Headquarters Services, Directorate for Information Operations and Reports (0704-0188), 1215 Jefferson Davis Highway, Suite 1204, Arlington, VA 22202-4302. Respondents should be aware that notwithstanding any other provision of law, no person shall be subject to any penalty for failing to comply with a collection of information if it does not display a currently valid OMB control number.
PLEASE DO NOT RETURN YOUR FORM TO THE ABOVE ADDRESS.

1. REPORT DATE *(DD-MM-YYYY)*	2. REPORT TYPE	3. DATES COVERED *(From - To)*
01-07-2019	Final	From 31-01-2018 to 30-06-2019

4. TITLE AND SUBTITLE
Development of a Novel Janus Hollow Fiber Membrane-Based Direct Contact Membrane Distillation (DCMD) Desalination Process for the Treatment of High Salinity Flowback and Produced Water

5a. CONTRACT NUMBER
Agreement No. R17AC00143

5b. GRANT NUMBER

5c. PROGRAM ELEMENT NUMBER

6. AUTHOR(S)
Jianjia Yu, Lusi Zou, and Guoyin Zhang

5d. PROJECT NUMBER

5e. TASK NUMBER

5f. WORK UNIT NUMBER

7. PERFORMING ORGANIZATION NAME(S) AND ADDRESS(ES)
Petroleum Recovery Research Center
New Mexico Institute of Mining and Technology
801 Leroy Place
Socorro, NM 87801

8. PERFORMING ORGANIZATION REPORT NUMBER

9. SPONSORING/MONITORING AGENCY NAME(S) AND ADDRESS(ES)
Bureau of Reclamation
U.S. Department of the Interior
Denver Federal Center
PO Box 25007, Denver, CO 80225-0007

10. SPONSOR/MONITOR'S ACRONYM(S)
Reclamation

11. SPONSOR/MONITOR'S REPORT NUMBER(S)
DWPR Report No. 223

12. DISTRIBUTION/AVAILABILITY STATEMENT
Available from the National Technical Information Service,
Operations Division, 5285 Port Royal Road, Springfield VA 22161

13. SUPPLEMENTARY NOTES
Online at https://www.usbr.gov/research/dwpr/DWPR_Reports.html

14. ABSTRACT

In this study, an innovative Janus hollow fiber membrane (J-HFM) -based direct contact membrane distillation (DCMD) process was developed for desalination of actual produced water with elevated total dissolved solids (TDS) of 154,220 mg/L. Compared to neat PVDF hollow fiber membrane, the J-HFM showed both increased permeate water flux and improved energy efficiency with more than 99.99 percent salt rejection. The long-term desalination performance of the Janus-HFM was investigated via a 200-hour continuous DCMD experiment. The results showed that the permeate water flux declined from 25.41 kg/m^2h to 15.21 kg/m^2h, and the salt rejection was 98.4 percent at the end of the 200 hours of operation. It was found that both scales and dissolved organic matter induced foulants accumulated at the feed side of the membrane due to the complex composition of the produced water. Nonetheless, the desalination performance decline can be effectively inhibited from 40 percent to 9.7 percent with a simple physical cleaning process by using the permeate water that recovered in the DCMD process.

15. SUBJECT TERMS
Janus hollow fiber membrane, DCMD, Desalination, High-salinity, P/F water

16. SECURITY CLASSIFICATION OF:			17. LIMITATION OF ABSTRACT	18. NUMBER OF PAGES	19a. NAME OF RESPONSIBLE PERSON
a. REPORT	b. ABSTRACT	THIS PAGE			Dr. Anthony Kennedy
U	U	U			19b. TELEPHONE NUMBER *(Include area code)* (303) 445-3230

Desalination and Water Purification Research and Development Program Report No. 223

Development of a Novel Janus Hollow Fiber Membrane-Based Direct Contact Membrane Distillation Desalination Process for the Treatment of High Salinity Flowback and Produced Water

Prepared for the Bureau of Reclamation Under Agreement Number R17AC00143

by:

Jianjia Yu, Lusi Zou, and Guoyin Zhang

New Mexico Institute of Mining and Technology

Mission Statements

The Department of the Interior conserves and manages the Nation's natural resources and cultural heritage for the benefit and enjoyment of the American people, provides scientific and other information about natural resources and natural hazards to address societal challenges and create opportunities for the American people, and honors the Nation's trust responsibilities or special commitments to American Indians, Alaska Natives, and affiliated island communities to help them prosper.

The mission of the Bureau of Reclamation is to manage, develop, and protect water and related resources in an environmentally and economically sound manner in the interest of the American public.

Disclaimer

The views, analysis, recommendations, and conclusions in this report are those of the authors and do not represent official or unofficial policies or opinions of the United States Government, and the United States takes no position with regard to any findings, conclusions, or recommendations made. As such, mention of trade names or commercial products does not constitute their endorsement by the United States Government.

Acknowledgements

This research was financially supported by the Bureau of Reclamation under its Desalination and Water Purification Research and Development Program (DWPR) through agreement number R17AC00143, and the Petroleum Recovery Research Center (PRRC) of the New Mexico Institute of Mining and Technology.

Acronyms and Abbreviations

Acronym or Abbreviation	Definition
AG	air gap
API	American Petroleum Institute
ATR-FTIR	attenuated total reflection-Fourier-transform infrared spectroscopy
BET	Brunauer-Emmett-Teller
CBM	coal bed methane
CR	collecting rate
DCMD	direct contact membrane distillation
DI	deionized water
DWPR	Desalination and Water Purification Research and Development Program
EC	electrical conductivity
EDX	energy-dispersive x-ray spectroscopy
F/P water	flowback and produced water
FESEM	field emission scanning electron microscope
FTIR	Fourier-transform infrared spectroscopy
IC	ion chromatography
IUPAC	International Union of Pure and Applied Chemistry
J-HFM	Janus hollow fiber membranes
LEP	liquid entry pressure
MD	membrane distillation
NMP	N-Methyl-2-pyrrolidone
NPOC	non-purgeable organic carbon
O&G	oil and grease
PEG	polyethylene glycol
PES	polyethersulfone
PP	polypropylene
PRRC	Petroleum Recovery Research Center
PTFE	polytetrafluoroethylene
PVA	polyvinyl alcohol
PVDF	polyvinylidene fluoride
Reclamation	Bureau of Reclamation
RO	reverse osmosis

Acronym or Abbreviation	Definition
SEM	scanning electron microscope
Si-R	silica nanoparticle modified by alkyl group
SMM	surface modifying molecules
SS	suspended solid
TDS	total dissolved solid
TEOS	tetraethyl orthosilicate
TMCS	trimethylchlorosilane

Measurements

Unit	Measurement
°F	degree Fahrenheit
°C	degree Celsius
nm	nanometer
µm	micrometer
cm	centimeter
µg/L	microgram per liter
g/L	gram per liter
ppm	parts per million
m/s	meter per second
cm/min	centimeter per minute
$kg/m^2/h$	kilogram per square meter per hour

Table of Contents

List of Figures

List of Tables

This page intentionally left blank.

Executive Summary

Direct contact membrane distillation (DCMD) has been regarded as a promising technology to treat high salinity flowback and produced (F/P) water. However, this process has not been widely used by the oil and gas industry in the last five decades. Important reasons contributing to its relatively limited use are its relatively lower water flux and its higher energy demand compared to the reverse osmosis process.

In this project, an innovative Janus hollow fiber membrane (J-HFM) -based DCMD process was developed for cost-effective and energy-efficient desalination of high salinity F/P water. Compared to a conventional hydrophobic membrane, the J-HFM consists of a superhydrophobic outer layer and a superhydrophilic inner layer which can help simultaneously improve mass transfer rate and inhibit heat transfer rate in the DCMD process, thereby achieving both enhanced water flux and reduced primary energy use.

Two different J-HFMs were prepared with the same hydrophobic outer layer (termed PVDF/Si-R) and two different hydrophilic inner layers (termed PVDF/PEG and PES/PEG) by using dip-coating and co-extruding methods, respectively. The effects of spinning and coating parameters on the membrane morphology were investigated. The results showed that the PES/PEG and PVDF/Si-R membrane consists of a transition layer with cellular sponge-like pores, and that the PVDF/PEG and PVDF/Si-R membrane was more suitable for the DCMD process due to its highly porous membrane structure with only interconnected pores.

Based on the PVDF/PEG and PVDF/Si-R J-HFMs, a series of DCMD experiments was carried out to optimize the operating conditions including feed salinity, temperature, feed flow velocity, permeate flow velocity, and flow mode. Compared to neat PVDF hollow fiber membrane, the J-HFM showed both increased permeate water flux and improved energy efficiency. The salt rejection was more than 99.9 percent.

The long-term desalination performance of the PVDF/PEG and PVDF/Si-R J-HFMs was investigated via a continuous 200-hour DCMD experiment. The results showed that the permeate water flux declined from 25.41 kilograms per square meter per hour ($kg/m^2/h$) to 15.21 $kg/m^2/h$, and that the salt rejection was 98.4 percent at the end of the 200 hours of operation. It was found that both scales and dissolved organic matter-induced foulants accumulated at the feed side of the membrane due to the complex composition of the produced water. Nonetheless, the desalination performance decline can be inhibited from 40 percent to 9.7 percent with a simple physical cleaning process by using the permeate water recovered in the DCMD process.

This page intentionally left blank.

1 Introduction

1.1 Project Background

Flowback and produced water (F/P water) is the largest volume liquid waste stream generated by the petroleum industry. Currently, the majority of F/P water generated from shale gas is re-injected via deep well injection. Therefore, treatment facilities are mainly designed to remove dispersed oil and grease (O&G) and suspended solids (SS) to avoid formation plugging. The F/P water treatment technologies applied in the petroleum industry focus primarily on using physical separation technologies, including the use of an American Petroleum Institute (API) standard oil-water separator, coalescing oil separator, or hydrocyclones. One crucial problem associated with physical separation is that it is challenging to transform the effluent from waste to a resource that can be recycled for petroleum stimulation or other beneficial reuse.

In recent years, extensive efforts have been made to explore advanced desalination technologies to cleanse F/P water to both reduce the disposal volume and provide a new viable water source for future well operations. Additional significant water conservation benefits include: (1) reduced injection volumes and diminished environmental impacts compared to current reinjection practices for F/P water; and (2) dramatic reductions in the required volumes of fresh water if F/P water can be treated and reused, since total dissolved solids (TDS) concentrations of F/P water can range from less than 3,000 mg/L in produced waters from coal bed methane (CBM) wells to more than 280,000 mg/L in produced waters from shale gas or oil wells. Desalination of this high-salinity impaired water has been regarded as a key challenge in the petroleum industry.

Direct contact membrane distillation (DCMD) is considered to be a promising technology for treating highly concentrated saline feed water. Owning to a low operating pressure, the DCMD process can be very tolerant of membrane fouling and only water vapor passes through the membrane pores (Li et al. 2017). Compared to conventional pressure-driven membrane-based separation processes such as nanofiltration and reverse osmosis, the driving force of DCMD is the difference in water vapor partial pressure across a porous hydrophobic membrane, which makes the DCMD process capable of treating high-salinity produced water (Hickenbottom and Cath 2014). It has been reported that salt rejection was independent of feed salinity in treating high salinity brines. For example, Minier-Matar et al. reported a flat-sheet polytetrafluoroethylene (PTFE) and polypropylene (PP) -based membrane distillation (MD) for the treatment of produced water from unconventional resources (Minier-Matar et al. 2014). They found that MD is feasible for desalinating brines from thermal desalination plants and can consistently produce high quality distillate; the membrane flux was not affected by salt

concentration of up to 70,000 mg/L. Singh et al. demonstrated a series of DCMD desalination processes with a PP hollow fiber membrane module (Singh et al. 2013). It was reported that the DCMD desalination process could be successfully employed to treat different kinds of produced water with very low TDS values in the distilled water and with 80 percent water recovery. The phenomenon of inorganic salt scaling was negligible in water recovered by membrane distillation. Macedonio et al. used a laboratory-made polyvinylidene fluoride (PVDF) hollow fiber membrane and commercial PP membrane-based DCMD desalination process to treat oilfield produced water (Macedonio et al. 2014). They found that DCMD showed excellent rejection of both total solids and carbon present in the produced water.

The major challenge associated with DCMD is the intensive energy requirement compared to conventional reverse osmosis (RO) processes (Al-Obaidani et al. 2008). The energy efficiency of DCMD is determined by several factors, such as feed water chemistry, water recovery, and heat source. The cost of DCMD has been reported to vary from \$0.3/m^3 to \$4.47 /m^3 for F/P water treatment (Elsayed et al. 2015; Singh and Sirkar 2012; Lokare et al. 2017). To improve the energy efficiency of DCMD, different types of low-grade heat sources, including solar thermal energy, geothermal energy, waste heat, and natural temperature gradient, have been used to make DCMD economically viable for large-scale desalination technology and competitive with commercially available RO (Ullah et al. 2018). As a promising alternative, the design of innovative Janus hollow fiber membranes (J-HFM), which can achieve both high mass transfer rate and low heat transfer rate, has attracted extensive attention in recent years.

1.2 Project Need

Figure 1 demonstrates the schematic structure of the J-HFM proposed for DCMD application.

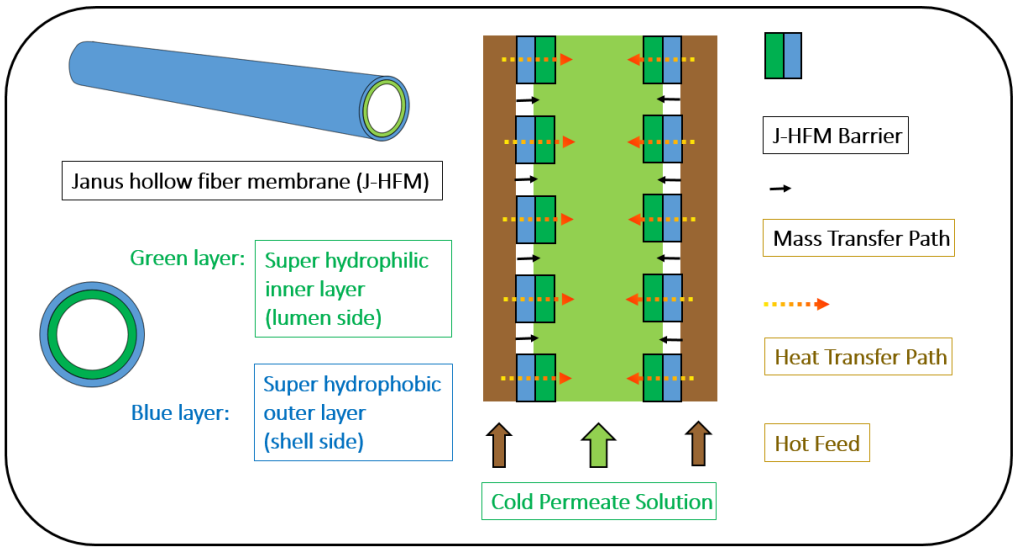

Figure 1. Schematic drawing of J-HFM for DCMD

J-HFMs have been widely characterized as super-hydrophobic and super-hydrophilic composite hollow fiber membranes. During the DCMD desalination process, the super-hydrophobic layer facing the hot side avoids the direct contact between high salinity feed water and the permeate water, allowing transport of water vapor through the pores. The mass transfer of water vapor is expressed in equation (1) (Phattaranawik et al. 2003; Qtaishat et al. 2008):

$$J_w = \boldsymbol{k_m}\left(p_{f,m} - p_{p,m}\right) \qquad (1)$$

where J_w is the water flux, k_m is the membrane permeability, and $p_{f,m}$ and $p_{p,m}$ are the water vapor partial pressures at feed side and permeate side, respectively. The membrane permeability is dependent on membrane characteristics and is always inversely proportional to the thickness of the membrane. The relationship between membrane permeability and membrane thickness for a typical Knudsen flow can be described using the following equation (Phattaranawik et al. 2003; Qtaishat et al. 2008):

$$k_m = \frac{2\varepsilon r}{3\tau\delta_m}\left(\frac{8M}{\pi RT}\right)^{1/2} \qquad (2)$$

where ε is the surface porosity, r is the pore radius, τ is the pore tortuosity, δ_m is the membrane thickness of the hydrophobic membrane, M is the molecular weight of the water, R is the gas constant, and T is the absolute temperature.

Compared to the conventional hydrophobic membrane, it is obvious that the thickness of the hydrophobic layer can be effectively reduced by the introduction of a relatively thick porous hydrophilic layer. During the DCMD process, the hydrophobic layer is expected to be filled with the permeate water from the cold permeate side, which helps reduce the mass transfer resistance across the membrane and thus improves the water flux.

During the water permeation process, a considerable amount of heat is transported through the membrane, which mainly consists of conductive heat transport across the membrane material (Q_c) and latent heat of vaporization associated with the water vapor transport through the membrane pores (Q_N). The latent heat is the effective heat that can be used to drive the DCMD process, and the energy efficiency is expressed as the ratio of the latent heat to the total heat, as expressed in the following equations (Zhang et al. 2010):

$$Q_v = J_w \cdot \Delta Hv \qquad (3)$$

$$Q_c = \frac{\gamma_m}{\delta_m}\left(T_{f,m} - T_{p,m}\right) \qquad (4)$$

$$EE(\%) = \frac{J_w \cdot \Delta Hv}{J_w \cdot \Delta Hv + \frac{\gamma_m}{\delta_m}(T_{f,m} - T_{p,m})} \times 100 \qquad (5)$$

where ΔHv is the latent heat of vaporization and γ_m is the thermal conductivity of the membrane.

Similar to equation (2), the conductive heat is also inversely proportional to the membrane thickness. This means that the reduction of membrane thickness promotes the heat transfer from the hot feed side to the cold permeate side, and that the effective heat used for the water evaporation may be significantly sacrificed. Thus, the presence of a thick hydrophilic layer in the J-HFM can help maintain membrane thickness and provide additional resistance for heat conduction through the membrane (equations 1 through 5).

J-HFMs can be directly fabricated by dual-layer composite or single-sided modification protocols. Khayet *et al.* reported a novel and simple method to prepare the hydrophilic/hydrophobic flat-sheet composite porous membranes by introducing fluorinated surface modifying molecules (SMMs) into a hydrophilic polymer matrix with a phase inversion method (Khayet et al. 2005; Khayet et al. 2006). Compared to the conventional hydrophobic membrane, their proposed membrane possessed a thinner hydrophobic porous top layer responsible for the water vapor transport in DCMD and a thicker hydrophilic porous sub-layer filled with water to lower the conductive heat loss. Bonyadi and Chung introduced a co-extrusion spinning process for the fabrication of dual-layer hydrophilic/hydrophobic hollow fiber membranes by using PVDF and cloister clay particles for DCMD desalination (Bonyadi and Chung 2007). It was found that the optimization of membrane characteristics can significantly enhance the obtained water flux in the DCMD desalination process. Similarly, PVDF/polyvinyl alcohol (PVA) hydrophobic/hydrophilic composite hollow fiber membranes were also reported for DCMD desalination (Zhu et al. 2015). The phenomenon of the penetration of sodium chloride solution into the membrane pores was thoroughly investigated in terms of membrane morphology and pore wetting during the DCMD process.

Considering that the most recent studies of J-HFM are mainly designed to desalinate impaired water with relatively low salinities, and that energy efficiency is rarely viewed as a critical parameter in the DCMD process, the design and manufacture of novel J-HFMs are still needed to desalinate high salinity water in a cost-effective way that can reduce primary energy use.

1.3 Project Objective

In this project, we aimed to develop a novel J-HFM-based DCMD process for desalination of a high-salinity produced water with a TDS concentration of 154,220 mg/L. The objectives of this study included: (1) to fabricate J-HFMs comprising a thin superhydrophobic outer layer and a thick porous hydrophilic inner layer; (2) to carry out long-term DCMD experiments by using

actual high-salinity produced water as feed solution and investigating the desalination performance of J-HFM in terms of permeate water flux, salt rejection, and specific energy consumption; and (3) to evaluate long-term stability and desalination performance recovery of the J-HFM thorough a physical cleaning process by using permeate water derived from the DCMD process.

2 Technical Approach and Methods

2.1 Preparation of Superhydrophobic Silica Nanoparticles

Superhydrophobic silica nanoparticles (Si-R) were first prepared with a sol-gel method. Briefly, 52.08 g of tetraethyl orthosilicate (TEOS) and 10.375 g of hydrochloric acid (HCl, 1.0 M) were added into 50 mL N-methyl-2-pyrrolidone (NMP) in a three-neck round-bottom flask under magnetic stirring. The hydrolysis of TEOS occurred at room temperature for 12 hours until a transparent silica sol was obtained. The silica sol was then modified with 13.50 g of trimethylchlorosilane (TMCS) at a specific temperature between 60°C and 100°C for 4 hours, which produced TMCS-modified Si-R nanoparticles. The formation mechanism of the superhydrophobic Si-R nanoparticle is shown in Figure 2.

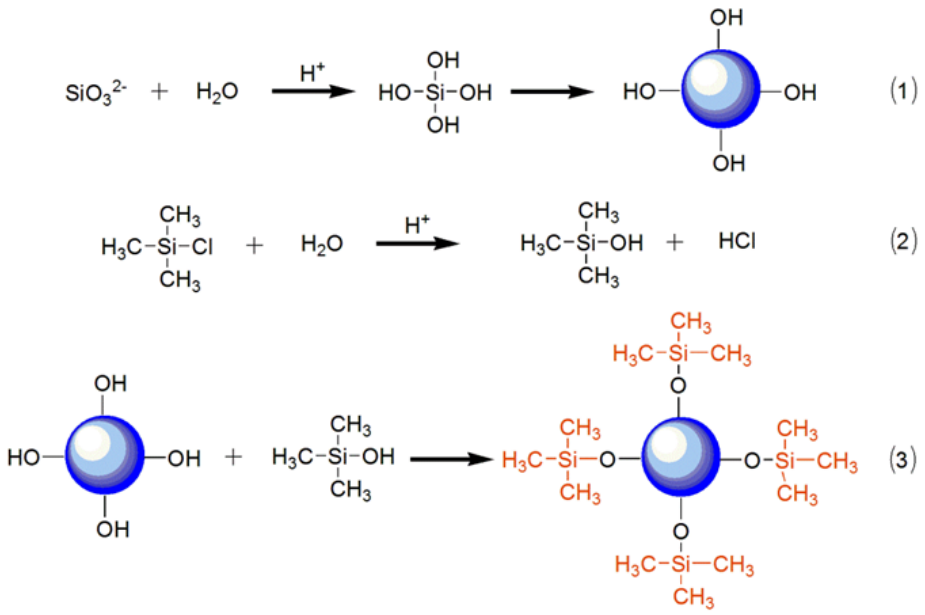

Figure 2. Formation mechanism of super hydrophobic Si-R nanoparticles

2.2 Preparation of PES/PEG and PVDF/Si-R Dope Solutions

Polyethersulfone (PES) pellets were directly dissolved into N-Methyl-2-pyrrolidone (NMP) solvent under mechanical stirring at ambient temperature. During the mixing process, polyethylene glycol (PEG 600) was added as pore agent to prepare a PES/PEG dope solution. The resulting homogeneous PES/PEG dope solution was degassed in a vacuum oven for future use.

Similarly, a PVDF/Si-R dope solution was prepared as follows: a specific quantity of Si-R nanoparticles was dissolved in NMP to obtain a transparent brown solution. PVDF powder was then added to the brown solution under mechanical stirring to form a homogeneous PVDF/Si-R dope solution. The air bubbles in the dope solution were removed in a vacuum oven to prepare it for future use.

2.3 Fabrication of Janus Hollow Fiber Membranes

2.3.1 Dip Coating Method

PES hollow fiber membrane was first fabricated by co-extrusion and dry jet wet spinning phase inversion technique. The apparatus for hollow fiber membranes fabrication is shown in Figure 3. Briefly, PES/PEG dope solution and bore-fluid (NMP/water) were simultaneously extruded through a spinneret with two ISCO syringe pumps. The flow rate was set at 2.0 mL/min and 1.0 mL/min for the PES/PEG dope solution and the NMP/water bore fluid, respectively. The air gap between the spinneret and the water coagulation bath was controlled. PES/PEG hollow fiber membrane was formed in the water coagulation bath and then was transported over several rollers to be collected in a water bath. The collecting velocity of the hollow fiber membranes was controlled by a rotary pump that equipped with a large-diameter drum in the water bath. The spinning parameters for PES/PEG hollow fiber membrane are listed in Table 1.

The obtained hollow fiber membranes were first immersed in water for two days to remove the solvent, and then soaked sequentially in methanol and hexane to completely remove residual water from the membrane.

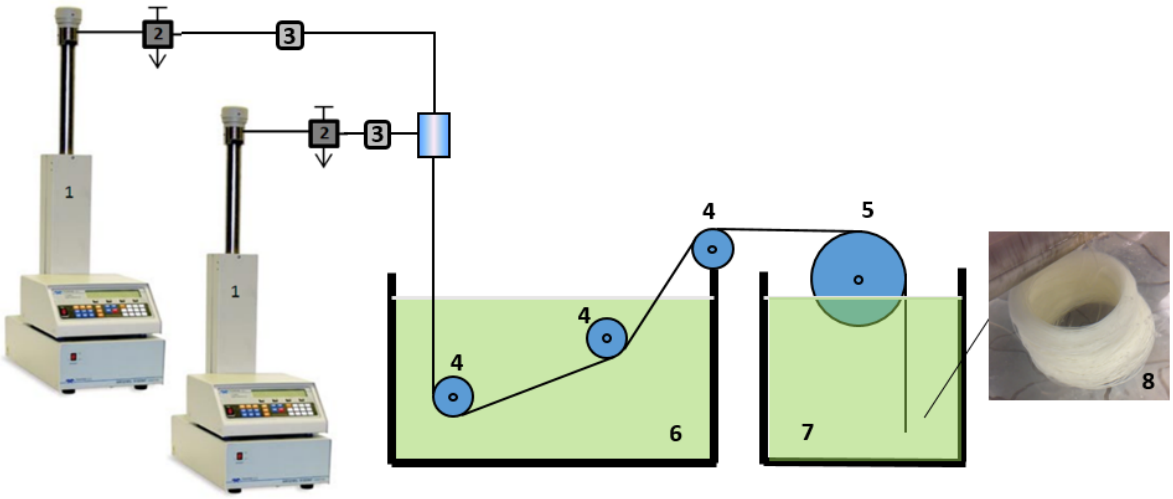

Figure 3. Schematic diagram for PES/PEG hollow fiber membrane fabrication: (1) ISCO pump; (2) three-way valve; (3) filter; (4) Teflon roller; (5) collection drum; (6) water coagulation bath; (7) water bath; (8) hollow fiber membranes

Table 1. Parameters for the fabrication of hydrophilic PES hollow fiber membranes

Parameter	Value
Dope composition	29% PES, 6% PEG 600
Bore fluid composition (%)	NMP/water=10/90
External coagulation bath	Water
Air gap (cm)	1, 3, and 5
Dope solution flow rate (mL/min)	2.0
Bore solution flow rate (mL/min)	1.0
Collecting velocity (cm/min)	200 and 400

The PES/PEG hollow fiber membrane was then soaked in PVDF/Si-R dope solutions (12 percent and 16 percent) for 10 seconds to acquire the superhydrophobic and superhydrophilic PES/PEG and PVDF/Si-R J-HFMs.

2.3.2 Co-Extruding Method

In addition to the dip coating method, a simultaneously coextruding of PVDF/PEG and PVDF/Si-R dope solutions through a triple-orifice spinneret was also used to fabricate the J-HFMs, as shown in Figure 4; the membrane spinning parameters are listed in Table 2.

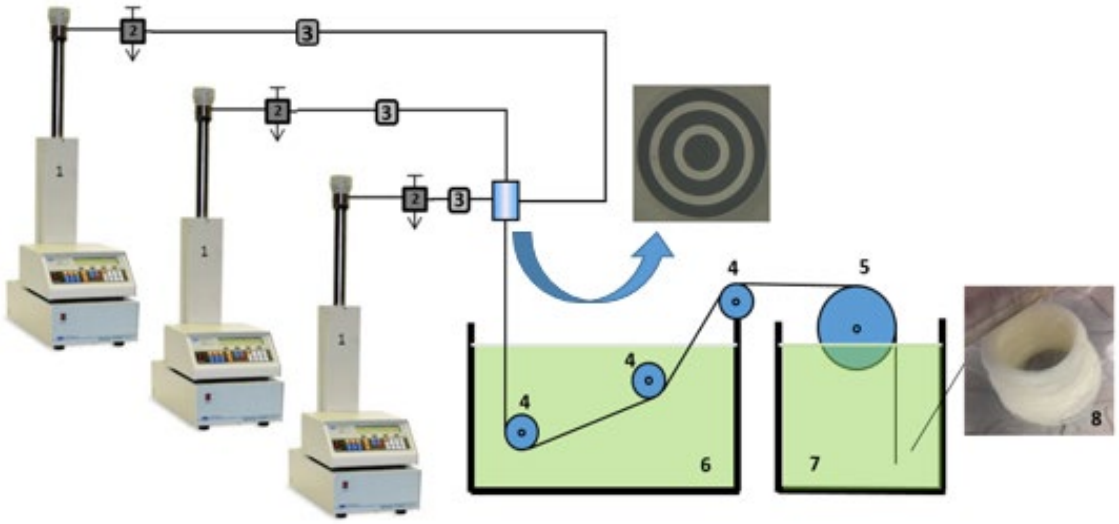

Figure 4. Schematic diagram for J-HFM fabrication via co-extruding method: (1) ISCO pump; (2) three-way valve; (3) filter; (4) Teflon roller; (5) collection drum; (6) water coagulation bath; (7) water bath; (8) hollow fiber membranes

Table 2. Parameters for the fabrication of the J-HFMs

Parameter	Value
Outer Layer Dope Composition	PVDF/Si-R/NMP (12/1/87)
Inner Layer Dope Composition	PVDF/PEG/NMP (12/6/82)
Bore fluid	NMP/water (70/30)
External coagulant	Tap water
Outer layer flow rate (mL/min)	2
Inner layer flow rate (mL/min)	2
Bore flow rate (mL/min)	2
Length of the air gap (cm)	5
Take-up speed	Free fall

2.4 DCMD Desalination Experiment for Produced Water Treatment

The apparatus for the direct contact membrane distillation (DCMD) process is shown in Figure 5. The feed solution was heated in a water bath and then pumped into the shell side of the hollow fiber membrane; deionized (DI) water was cooled and circulated at the lumen side of the membrane. Temperature was recorded with four digital temperature sensors at the inlets (Tf, 1 and Tp, 1) and outlets (Tf, 2 and Tp, 2) of the membrane module. Two Masterflex peristaltic

pumps were used to adjust flow rates for the feed solution and the cold DI water. The masses of the hot feed solution and cold permeate water were weighed, using two digital scales equipped with a data acquisition system, to measure real-time fresh water harvest in the cold permeate side. Both electrical conductivity (EC) and total dissolved solids (TDS) in the permeate water were measured with a TDS/conductivity meter (Hach HQ40d) to evaluate salt rejection in the DCMD process.

The permeate water flux of the DCMD process was measured by recording the mass of water received at the cold permeate side per equation (6). Energy efficiency was evaluated by monitoring the feed temperature at both the inlet and outlet as described in Equation (7) (Khayet et al. 2005):

$$J_w = \frac{\mathrm{W}}{\mathrm{A} \times \mathrm{t}} \qquad (6)$$

$$EE(\%) = \frac{J_w \Delta H A}{F C_p (T_{f,in} - T_{f,out})} \qquad (7)$$

where Jw is the permeate water flux (kg/m^{2}h), W is the mass of water received at the cold permeate side (kg), A is the effective membrane area (m^2), t is operating time (h), ΔH is the latent heat of water evaporation (2257 kJ/kg), F is the mass flow rate of the feed solution (kg/s), and Tf, in and Tf, out are the temperatures of the feed solution at the inlet and outlet (K), respectively.

Figure 6 illustrates the assembly of the J-HFM module through an epoxy-potting technique. Briefly, ten pieces of Janus hollow fiber membranes were bundled together through a ¼-inch stainless steel tubing with the two ends sealed by epoxy. The effective length of the J-HFM was 15 cm.

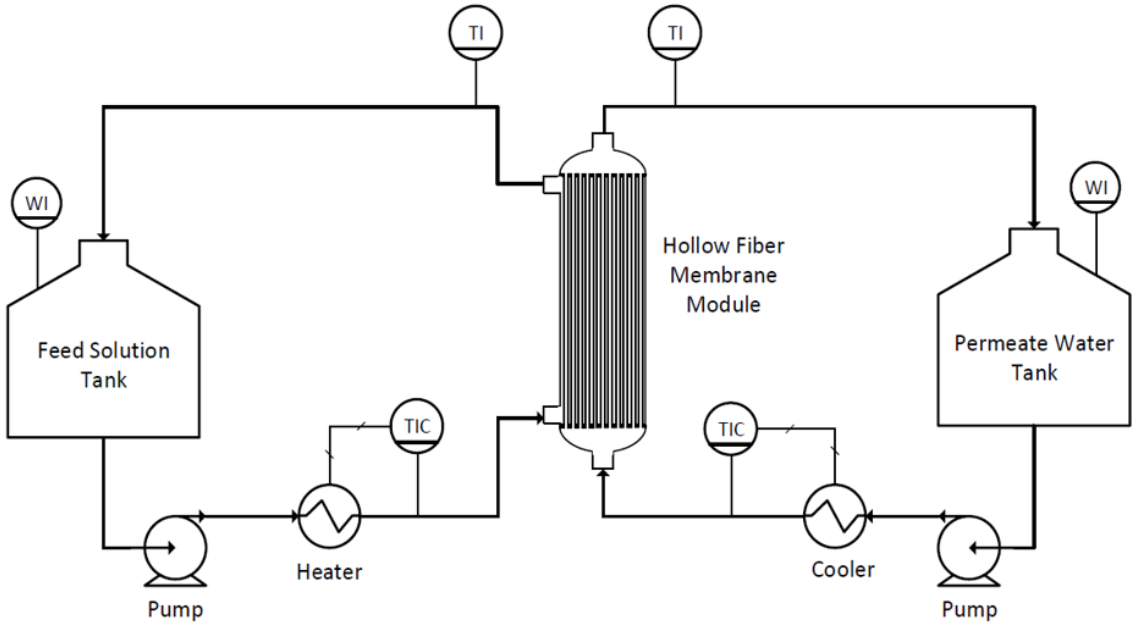

Figure 5. Experimental setup of the J-HFM DCMD process

Figure 6. J-HFM module

3 Results and Discussion

3.1 Characterization of Superhydrophobic Silica Nanoparticles

Fourier-transform infrared spectroscopy (FTIR; Nicolet™ iS50, Thermo Scientific, USA) was used to characterize silica nanoparticles before and after TMCS modification. The FTIR spectra of unmodified silica nanoparticle and the TMCS-modified nanoparticle are shown in Figure 7. This figure shows that both modified and unmodified silica show an absorption peak at 1080 cm^{-1}, which corresponds to the asymmetrical vibration of Si-O-Si. The adsorption peaks at 3400 cm^{-1} and 1600 cm^{-1} were observed in the spectrum of unmodified silica; this is attributed to the asymmetrical vibration of -OH on the surface of silica nanoparticle. Compared to the unmodified silica nanoparticle, the intensities of adsorption peaks at 3460 cm-1 and 1600 cm-1 were both reduced in the spectrum of modified silica. Furthermore, two new adsorption peaks appeared at 2969 cm^{-1} and 1450 cm^{-1}; these peaks are attributed to the asymmetrical vibration of C-H. The adsorption peaks at 1250 cm^{-1} and 850 cm^{-1} are attributed to the symmetrical vibration of Si-C. The decrease in adsorption intensity of -OH and the appearance of adsorption peaks of C-H and Si-C indicate that the silica was successfully modified.

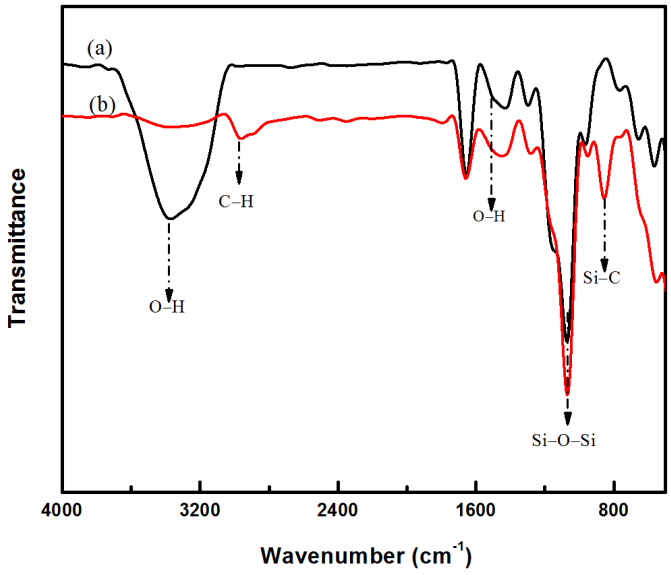

Figure 7. FTIR spectra of (a) unmodified silica nanoparticle; and (b) TMCS-modified Si-R nanoparticle

Figure 8 shows the solubility test of unmodified silica nanoparticles and the TMCS-modified Si-R nanoparticles in DI water. It can be seen that the unmodified silica nanoparticles are completely dissolved in DI water; however, the TMCS-modified Si-R nanoparticles cannot be dissolved. To further examine hydrophobicity of the TMCS-modified Si-R nanoparticles, the

contact angles of both unmodified silica nanoparticles and modified Si-R nanoparticles were measured with a contact angle system.

Figure 8. Solubility test of unmodified silica nanoparticles (left) and TMCS-modified Si-R nanoparticles (right) in water

Compared to unmodified silica nanoparticles, it can be seen in Figure 9 (a) that the contact angle of the TMCS-modified Si-R nanoparticle increased from 30.5°C to 136.3°C. Figure 9 (b) shows the contact angles of the Si-R nanoparticles modified under different temperature. The results indicate that temperature plays an important role in the TCMS modification process. The modified Si-R nanoparticles show contact angles of 112.5°C, 136.3°C, and 127.6°C at temperatures of 60°C, 80°C, and 100°C, respectively. It is believed that the TMCS could not be completely reacted with silica sol under low temperature. However, if the temperature is too high, the hydrolytic TMCS and TEOS may self-dehydrate and even become self-cross-linked during the modification process.

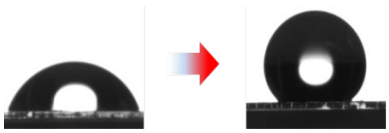

(a)

Figure 9. Contact angle measurements (a) of unmodified silica nanoparticle (left) and FMCS-modified Si-R nanoparticle (right); and (b) contact angle of the TMCS-modified nanoparticles under different temperatures

3.2 Characterization of the PES/PEG and PVDF/Si-R Janus Hollow Fiber Membrane

The hollow fiber membranes were first frozen in liquid nitrogen and fractured with tweezers. Small pieces of hollow fibers were sputter-coated with platinum and then characterized by scanning electron microscope (SEM; S3200N, Hitachi).

Figure 10 shows SEM images of cross sections of PES/PEG and PVDF/Si-R J-HFM. These images show that the J-HFMs demonstrate an asymmetric morphology characterized by a thin skin and a porous bulk that comprises fully-developed macropores extending to the central portion or even toward the bottom region of the membrane. The diameter of the J-HFM is around 986 µm. The average thickness of the PES/PEG inner layer is 156 µm and the average thickness of the PVDF/Si-R outer layer is 32 µm. It is interesting to note that there is a transitional layer

formed between the PES/PEG inner layer and the PVDF/Si-R outer layer; the thickness of the transitional layer is around 59 µm. The details of the three layers are presented in high resolution SEM images with different magnifications, as shown in Figure 10.

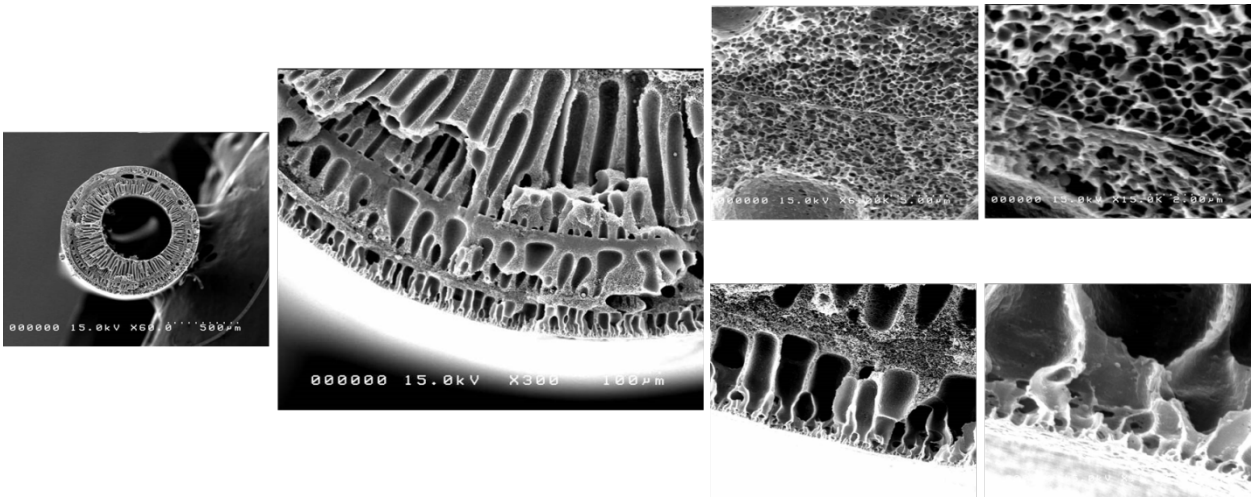

Figure 10. Cross-sectional images of PES/PEG and PVDF/Si-R J-HFM

The PES/PEG inner layer functions as a hydrophilic supporting layer, consisting of both finger-like pores and sponge-like pores. With PVDF/Si-R dope solution coated on the outer surface of the PES/PEG substrate, a PVDF/Si-R layer was formed around the outside of the substrate. The PVDF/Si-R outer layer shows a porous structure with macrovoids beneath the outer surface; this is attributed to an instantaneous liquid-liquid demixing between NMP and water in the phase inversion process. The solvent-nonsolvent exchange rate was slowed in the presence of the PVDF/Si-R outer layer, and the liquid-liquid demixing process was delayed, resulting in the formation of a transitional layer that comprises both cellular sponge-like micropores and pyriform-like macrovoids between the PVDF/Si-R outer layer and the PES/PEG inner layer, as shown in Figure 10 (second image from left).

In Figure 10, the two images on the upper right depict pore structure at the interface between the PES/PEG inner layer and transition layer, and the two images on the lower right depict that interface between the transition layer and the PVDV/Si-R outer layer. These images show that only sponge-like pores are found at the interface; the layers are well attached without any delamination.

3.2.1 Effects of Air Gap and Collecting Rate on Morphology of the J-HFM

Compared to flat sheet membrane, the formation mechanism of hollow fiber membrane is more complex. There are many factors influencing the ultimate membrane morphology and performance of the hollow fiber membranes. The distance of air gap (AG) and hollow fiber collecting rate (CR) have been taken into account to discuss effect of spinning conditions on the formation mechanism of the J-HFMs.

Figure 11 shows SEM images of cross sections of the J-HFMs fabricated at different AG distances. It can be seen that a PVDF/Si-R layer is well-formed around the outer surface of the PES/PEG substrate for all the J-HFMs. The amount of the pyriform-like macrovoids in the PVDF/Si-R layer tends to decrease with the increased AG distance. Due to an enhanced molecular orientation and polymer chain package, the surface layer of the PES/PEG substrate becomes denser and the porosity decreases with increasing AG, resulting in a delayed demixing process during the dip coating process. The slowed liquid-liquid exchange rate inhibits the formation of macrovoids at the PVDF/Si-R layer.

Figure 11. SEM images of cross-sections of the PES/PEG and PVDF/Si-R J-HFM at different AG distances (CR = 200 cm/min): top row AG = 1 cm; center row AG = 3 cm; bottom row AG = 5 cm

Hollow fiber CR plays an important role in determining the final dimensions of the hollow fiber membranes, especially diameter and thickness. Figure 12 presents SEM images of cross-sections of the PES/PEG substrate and the J-HFM at different CRs. With the CR increased from 200

cm/min to 400 cm/min, the diameter of the PES/PEG substrate declined from 876 µm to 668 µm, and the membrane thickness decreased from 168 µm to 154 µm. The images also show that the PVDF/Si-R layer was well coated without any delamination between the PES/PEG substrate and the PVDF/Si-R layer; a thicker microsponge-like PVDF/SiO2 layer was formed when the collecting rate was 400 cm/min.

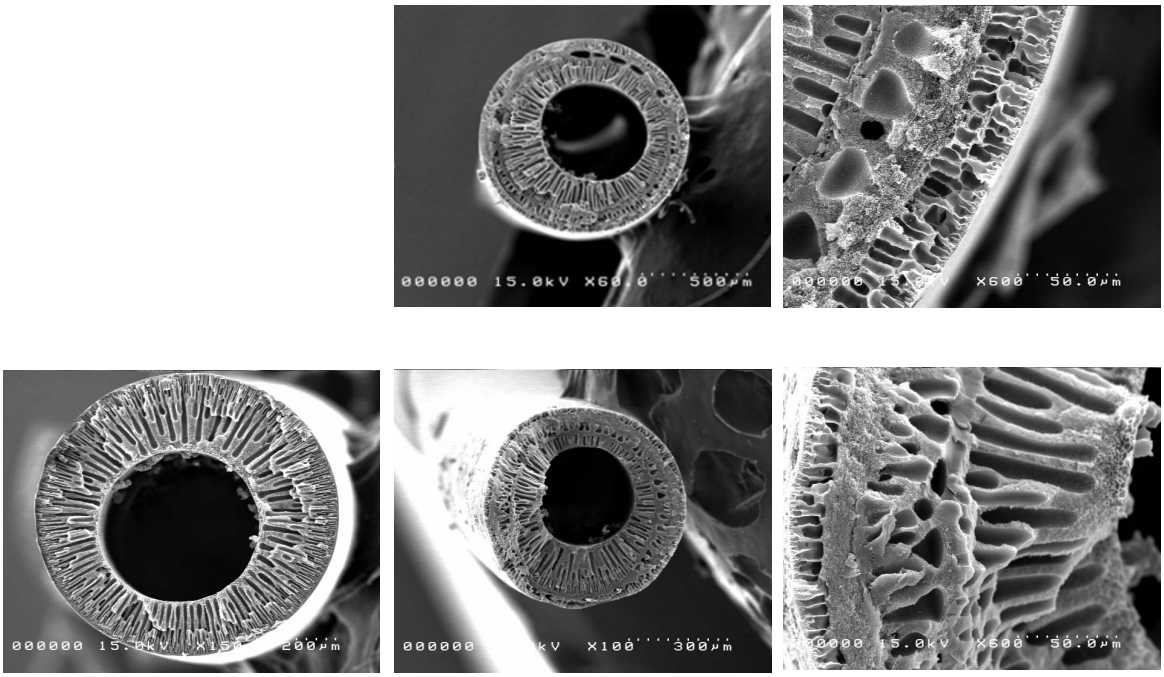

Figure 12. SEM images of cross-sections of the PES/PEG HFM and the PES/PEG and PVDF/Si-R J-HFM (AG = 1 cm); CR = 200 cm/min for images in the top row; CR = 400 cm/min for images in the bottom row

3.2.2 Effects of Dope Concentration and Coating Time on Morphology of the J-HFM

Figure 13 shows the effect of PVDF/Si-R dope concentration on morphology of the J-HFM where the coating time remains at 10 seconds. When the concentration was increased from 6 percent to 12 percent and 16 percent, the thickness of the PVDF/Si-R outer layer changed from 19 µm to 42 µm and 34 µm, respectively. The number of pyriform-like macrovoids decreased with the increase in PVDF/Si-R dope concentration, since macrovoids are usually associated with instantaneous precipitation. The reduced macrovoids may be attributed to the increased dope viscosity at higher PVDF/Si-R dope concentrations. During the nonsolvent-induced phase inversion process, viscosity has a strong influence on the interdiffusion of solvent and nonsolvent. High viscosity slows the rate of water penetration into the polymer matrix and the

delayed liquid-liquid demixing process prevents the formation of pear-like macrovoids at the PVDF/Si-R layer of the J-HFMs.

Figure 13. Effect of PVDF/Si-R concentration on morphology of the J-HFM; from left to right, images represent 6 percent, 12 percent, and 16 percent, respectively

Figure 14 depicts morphology of the J-HFMs coated with 16 percent PVDF/Si-R dope solution under different coating times. During the coating process, the PES/PEG substrate was first immersed into PVDF/Si-R dope solution; the coated membrane was then slowly passed through a small-diameter orifice for a specific time (in the air) before phase inversion in a water bath. The coating time refers to the time that the coated hollow fiber membrane was held in the air. Figure 14 shows that the thickness of the coated PVDF/Si-R layer increased from 34 µm to 44 µm when the coating time was extended from 10 seconds to 30 seconds. Compared to the membrane coated for 10 seconds, the membrane coated for 30 seconds exhibits a macrovoids-free transitional layer between the outer layer and the PES/PEG substrate.

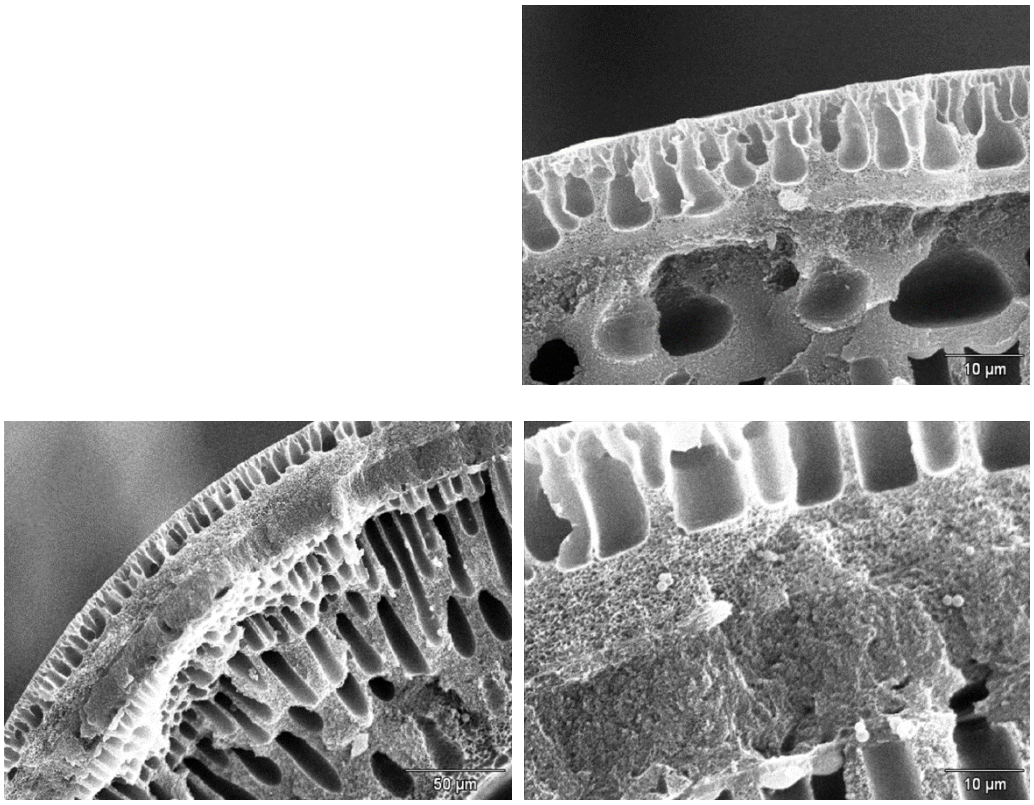

Figure 14. Effect of coating time on morphology of the J-HFM; images in the top row are for 10 seconds and images in the bottom row are for 30 seconds

3.2.3 Specific Surface Area and Porosity of the J-HFM

Brunauer-Emmett-Teller (BET) measurements were carried out at 77K using a nitrogen absorption-desorption based surface area analyzer (ASAP 2020, Micrometric USA) to assess specific surface area and pore size distribution of the hollow fiber membranes. Prior to the BET measurements, membrane samples were cut into small pieces and heated at 100°C under vacuum for 2 days to remove all residual moisture from the membranes.

Figure 15 shows the nitrogen adsorption-desorption isotherm and the pore size distribution of the J-HFM with different AG distances and CRs; the PVDF/Si-R concentration was 12 percent. According to IUPAC classification, the nitrogen adsorption/desorption isotherm exhibits an H1-type hysteresis loop, which indicates the presence of both macropores and mesopores in the membrane.

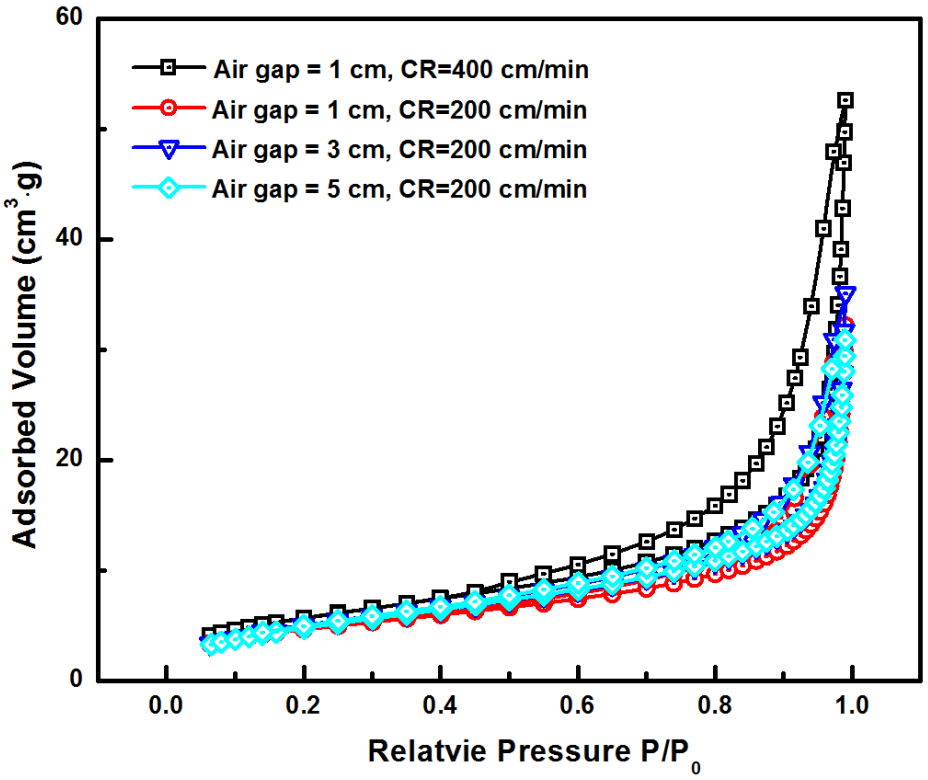

Figure 15. Nitrogen adsorption-desorption isotherm of the J-HFM with different AG distances and different CRs

Figure 16 shows pore size distribution of the J-HFM with the PES/PEG substrate fabricated at different AG distances and different CRs. The figure shows that the average pore size is distributed at two different intervals of 2 to 3 nm and 20 to 50 nm, with most pores possessing an average pore diameter between 29 and 38 nm. The average pore size decreases with increases in AG and CR. The result is consistent with previous SEM observations (Figure 11) that the formation of macrovoids was inhibited at increased AG distances. When the AG distance and CR are 5 cm and 400 cm/min, respectively, the amount of the small pores (dp = 2.8 nm) reaches the maximum.

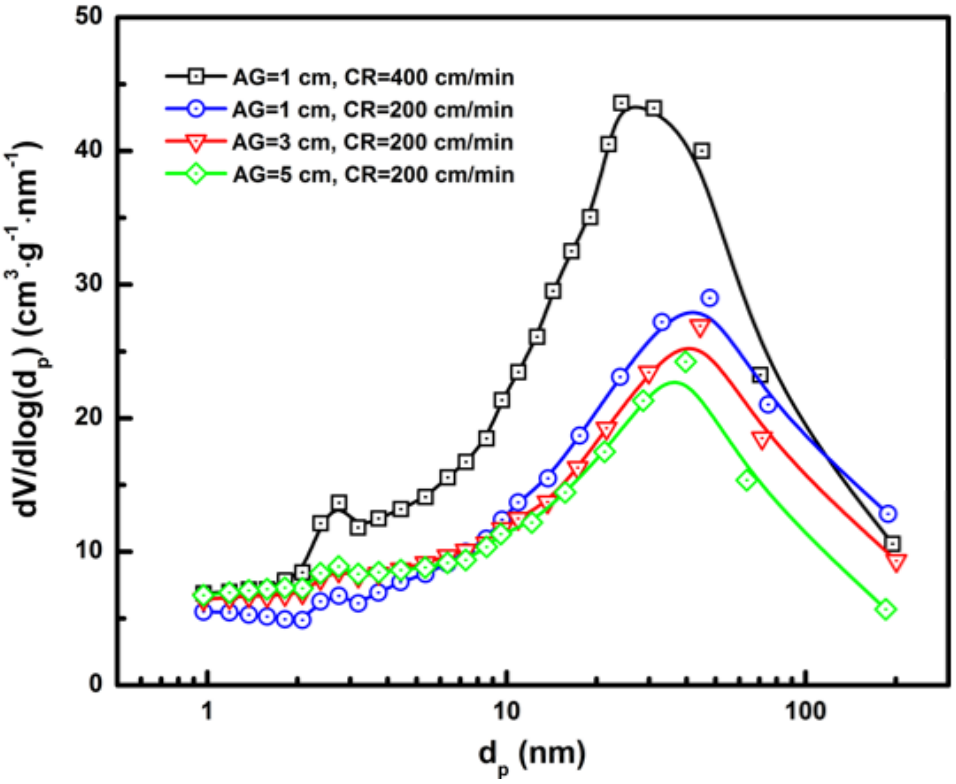

Figure 16. Pore size distribution of the J-HFM with different AG distances and different CRs

The concentration of PVDF/Si-R determines both thickness and micromorphology of the J-HFM. As noted previously, the number of pyriform-like macrovoids was reduced with increased PVDF/Si-R dope concentration. Figure 17 presents the pore size distribution of the J-HFM coated with different PVDF/Si-R concentrations. This figure clearly shows that the pore size distribution curve of the macropores shifted slightly to the left, which indicates a decreased average macro pore size. In addition, the amount of smaller pores (average pore diameter of 2.8 nm) increases with the increase in PVDF/Si-R dope concentration.

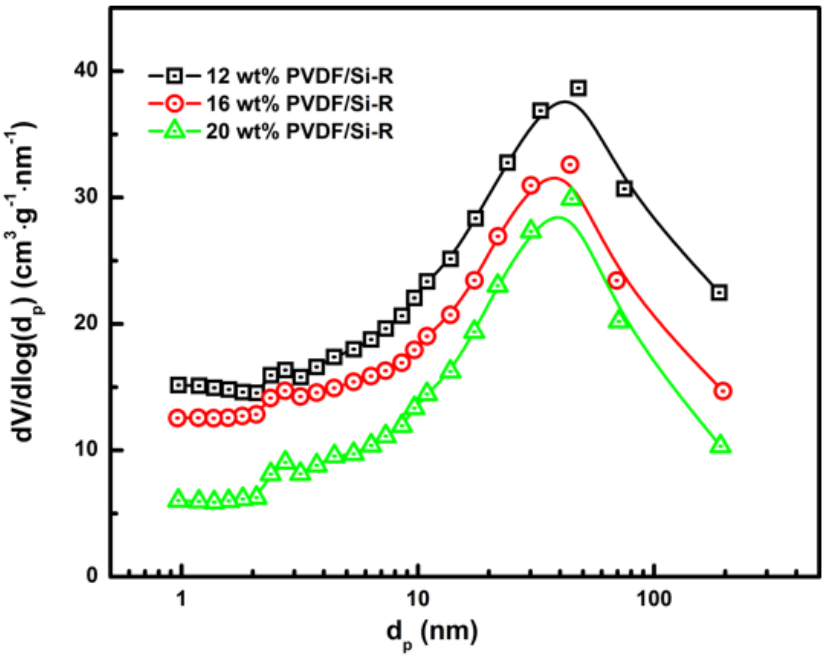

Figure 17. Pore size distribution of the J-HFM with different PVDF/Si-R concentration

Figure 18 shows the nitrogen adsorption-desorption isotherm and pore size distribution of the J-HFM with different contents of super hydrophobic nanoparticles in the PVDF/Si-R dope solution. The adsorption/desorption isotherms in these plots show that all the membranes possessed both micropores and mesopores. The impregnation of the super hydrophobic silica nanoparticles hindered the demixing process between solvent and nonsolvent, which resulted in reduced pore size in the J-HFMs.

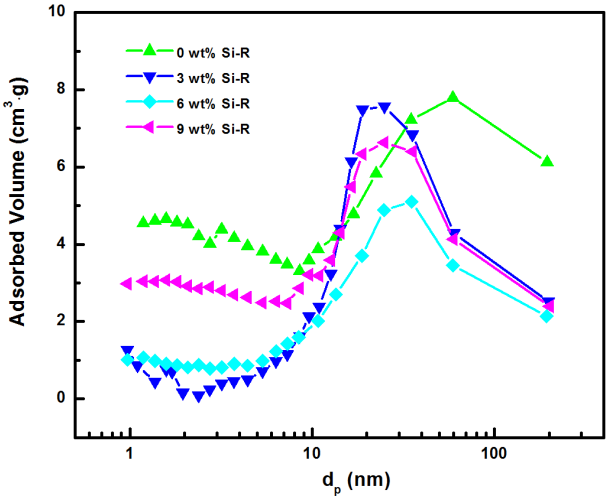

Figure 18. Nitrogen adsorption-desorption isotherm and pore size distribution of the J-HFM with different amounts of Si-R nanoparticles

3.2.4 Contact Angle Measurement

Figure 19 shows water contact angle measurements for three different hollow fiber membranes: PES/PEG hollow fiber membrane substrate; PVDF-coated PES/PEG hollow fiber membrane; and the PES/PEG and PVDF/Si-R J-HFM. The contents of PVDF and Si-R nanoparticles in the PVDF/Si-R dope solution were 12 percent and 3 percent, respectively. The figure shows that the neat PES/PEG hollow fiber membrane substrate had a water contact angle of 75.4°C. The water drop tends to penetrate into the hydrophilic PES/PEG substrate during the contact angle measurement. The contact angle of PES/PEG and PVDF/Si-R J-HFM showed a contact angle of 107.3°C, which is much higher than the contact angle (80.2°C) of the neat PVDF-coated PES/PEG hollow fiber membrane.

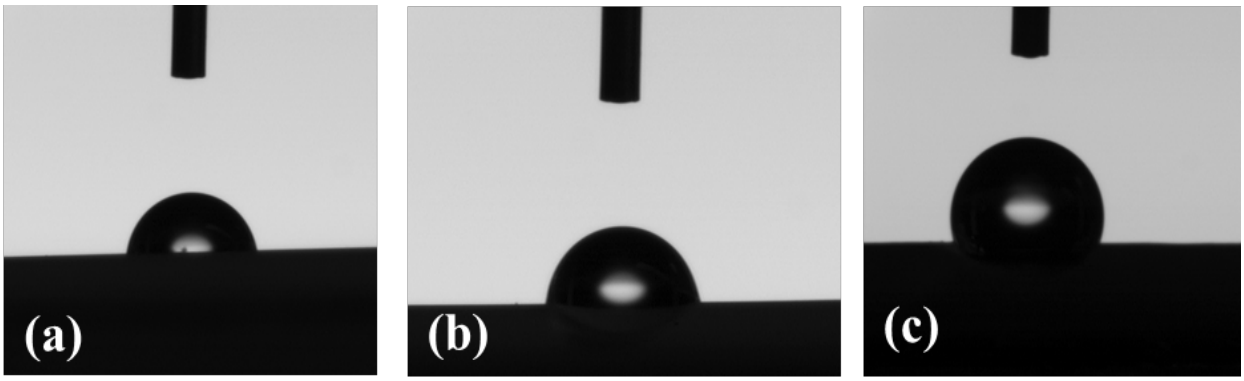

Figure 19. Water contact angle of (a) PES/PEG substrate; (b) PVDF coated PES/PEG hollow fiber membrane; and (c) PVDF/Si-R and PES/PEG J-HFM

3.3 Characterization of the PVDF/PEG and PVDF/Si-R J-HFM

Figure 20 (a) shows the micromorphology of the PVDF/PEG and PVDF/Si-R J-HFM. As clearly shown in the figure, the membrane exhibits an asymmetric structure with a thin and hydrophobic PVDF/Si-R outer layer and a thick and high-porous hydrophilic macrovoids-free PVDF/PEG inner layer, with the water contact angle of 137.6°C and 56.2°C at the outer surface and the inner surface, respectively.

In Figure 20 (b), large numbers of pyriform-like macrovoids are shown formed beneath the PVDF/Si-R outer surface. This is attributed to the different chemical composition of the two dope solutions; a similar phenomenon has been found by previous researchers (Ullah et al. 2018). In the process of phase inversion, and due to the presence of Si-R nanoparticles, the thermodynamic stability of the PVF/Si-R dope solution decreased and an instantaneous liquid-liquid demixing occurred to form the macrovoids under the surface of the outer layer. From a dynamic point of view, the superhydrophobic property of the Si-R nanoparticles can effectively impede the water diffusion to the PVDF/Si-R dope, which hinders the exchange between NMP and water. Thus, instead of a liquid-liquid demixing, the semi-crystalline PVDF experiences a

solid-liquid demixing and thus forms a porous nodular structure at the outer layer of the J-HFM (Guendouzi et al. 2001); this is shown in Figure 20 (c). The interconnected macrovoids-free PVDF/PEG inner layer is mainly from the increased dope viscosity due to the addition of PEG600 molecules to the PVDF dope solution, and also from the existence of 70 percent NMP in the bore fluid. Similar membrane morphology was reported by Wang et al. (Wang et al. 2017). It is interesting to note that the pore size decreased gradually from an average of 2 μm at the inner surface to an average of 0.15 μm on the outer surface.

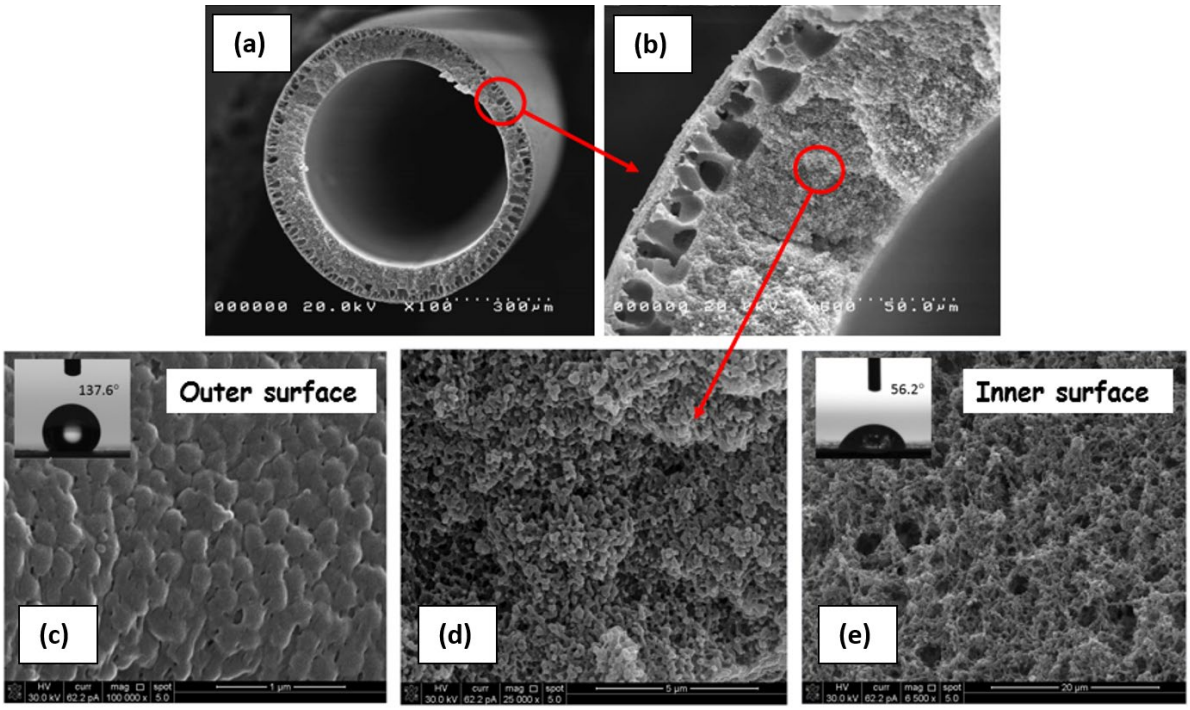

Figure 20. SEM images of the PVDF/PEG and PVDF/Si-R J-HFM

3.4 Performance of J-HFM Based DCMD Desalination Process

3.4.1 Selection of J-HFMs for DCMD Desalination

Two different J-HFMs were prepared with the same hydrophobic outer layer (PVDF/Si-R) and different hydrophilic inner layers (PVDF/PEG and PES/PEG) by using dip-coating and co-extruding methods, respectively. The two J-HFMs were used in the DCMD process and the desalination performances of the two membranes were then compared.

Figure 21 plots the mass of recovered permeate water during the DCMD process. As shown in the figure, the permeate water recovery continuously increased for the PVDF/PEG and PVDF/Si-R J-HFM, while it fluctuated up and down for the PES/PEG and PVDF/Si-R J-HFM. The corresponding permeate water flux was 23.4 kg/m^2/h and 1.86 kg/m^2/h, respectively, as shown in Table 3. When comparing the two J-HFMs, the PVDF/PEG and PVDF/Si-R showed an

interconnected microstructure with the pore size ranged from 0.15 µm to 2 µm. The high pore connectivity and porosity facilitate the transport of water vapor from the hydrophobic PVDF/Si-R outer surface to the hydrophilic PVDF/PEG inner surface. For the PES/PEG and PVDF/Si-R J-HFM, the diameter of most pores was less than 0.15 µm (Figure 16, Figure 17, and Figure 18) and it was difficult to eliminate the formation of the transition layer during the dip-coating process (Figure 10 through Figure 14). Thus, the permeate water flux was significantly inhibited from the dense transition layer with small cellular pores.

Table 3 also shows that the salt rejection of the two J-HFMs was higher than 99.9 percent, which indicated a good wetting resistance from the hydrophobic PVDF/Si-R layer of the J-HFMs. In view of the above comparison, the PVDF/PEG and PVDF/Si-R J-HFM was chosen for the DCMD desalination.

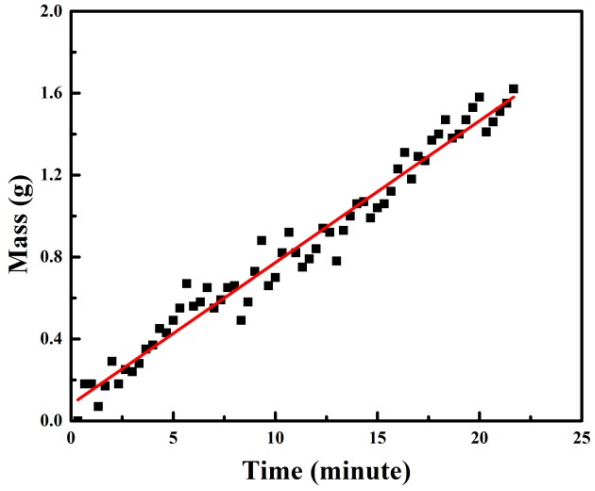

Figure 21. Mass changes of the permeate water from PVDF/PEG and PVDF/Si-R J-HFM (left) and from PES/PEG and PVDF/Si-R J-HFM (right)

Table 3. Desalination performance comparison for the two J-HFMs

Membrane	Temperature (°C)				Flux ($kg/m^2/h$)	Salt Rejection (%)
	Permeate In	Permeate out	Feed In	Feed Out		
PVDF/PEG and PVDF/Si-R J-HFM	20	60.2	79.5	72.8	23.4	99.98
PES/PEG and PVDF/Si-R J-HFM	20	64.5	80	73	1.86	99.92

Notes – Temperature T_f= 80 °C, T_p=20 °C; feed solution 3.5 wt% NaCl; feed velocity and permeate velocity 0.15 m/s and 0.5 m/s

3.4.2 Effect of Feed Salinity on Permeate Water Flux

The DCMD experiments were performed by using simulated produced water with salinities ranging from 10,000 ppm to 260,000 ppm. The feed solution was heated to 80°C and the DI water was cooled to 20°C. The flow rate was 0.15 m/s and 0.5 m/s for the feed solution and cold permeate water, respectively. Figure 22 shows mass changes of the permeate water as a function of time, when the DCMD process reached a steady state (after approximately 5 minutes) and temperatures were stable at the outlets for both feed solution and DI water. The plot shows that the amount of permeate water increased linearly with time and that the increased amount of the permeate water declined with increased feed salinity.

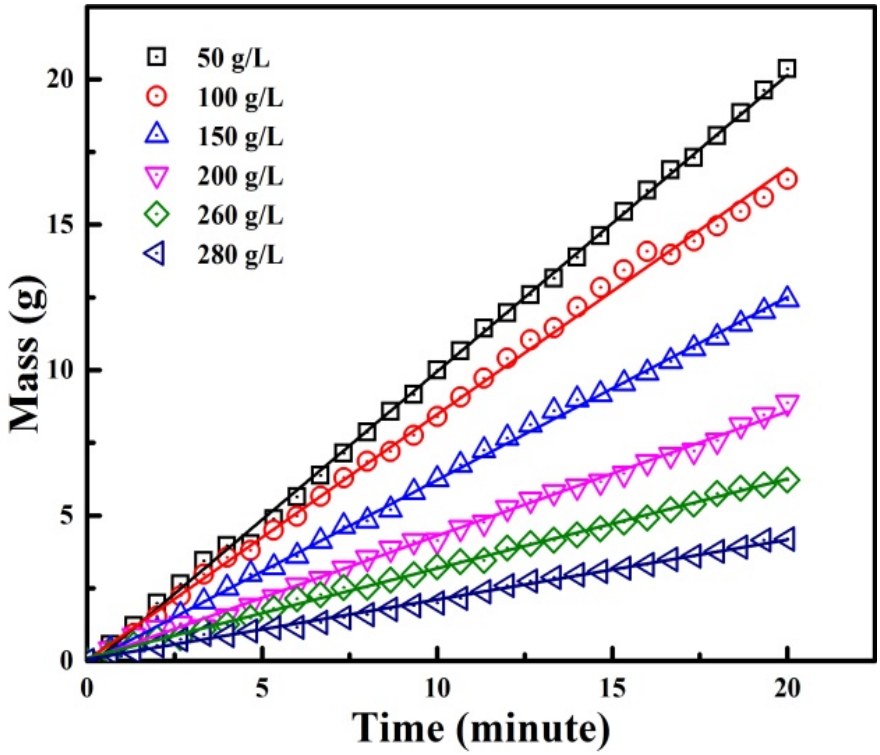

Figure 22. Mass changes of permeate water at different feed salinities

Figure 23 plots both permeate water flux and salt rejection of the J-HFM DCMD process at different feed salinities. When the feed salinity increased from 50,000 ppm to 280,000 ppm, the salt rejection slightly reduced from 99.98 percent to 99.58 percent and the permeate water flux decreased from 22.38 kg/m^{2}h to 4.50 kg/m^{2}h. The significant water flux reduction can be explained by the reduced partial vapor pressure at the hot feed side, thus reducing the driving force for the DCMD process. Similar results have been reported by Guendouzi et al, interpreted to mean that the partial vapor pressure reduced from the decreased water activity by the hydration of ion and ionic association in the feed solution (Guendouzi et al. 2001).

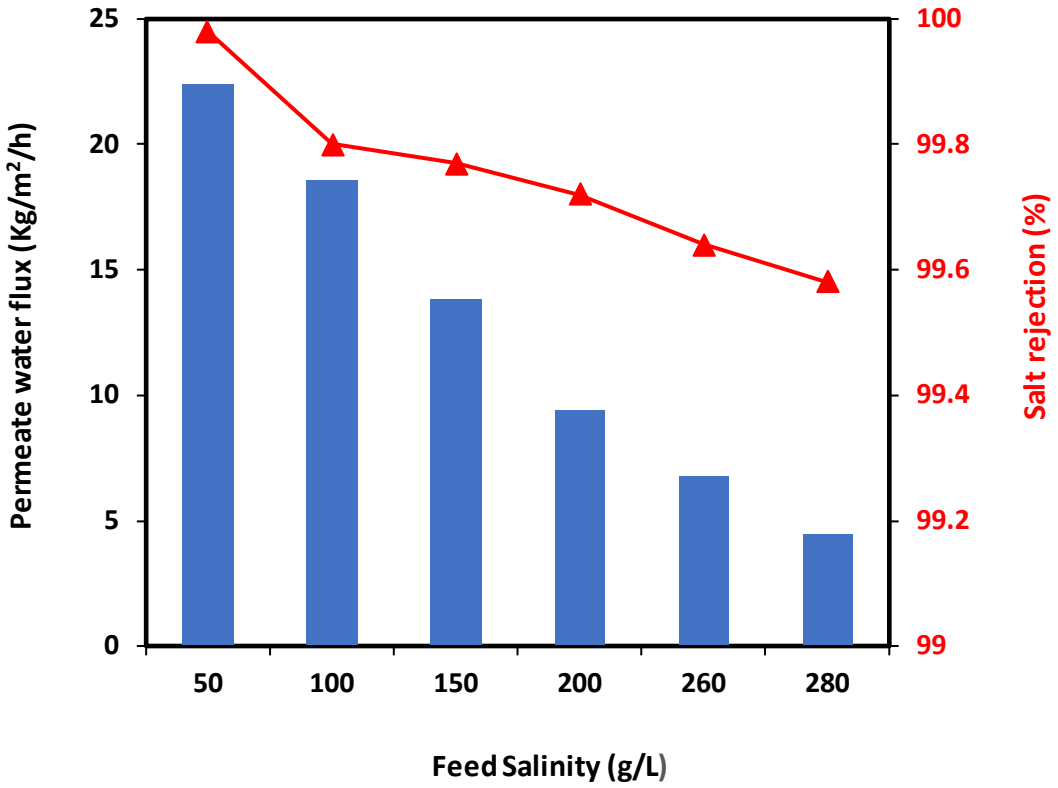

Figure 23. Effect of feed salinity on permeate water flux and salt rejection of the J-HFM DCMD process

3.4.3 Effect of Feed Temperature on Permeate Water Flux and Energy Efficiency

Figure 24 shows permeate water flux and temperature differential along the membrane at different feed temperatures. For this assessment, the feed salinity was fixed at 35,000 ppm, the temperature at the permeate side was 20°C, and the flow rates were 1.5 m/s and 0.15 m/s for the hot feed solution and the cold permeate water, respectively. As shown in Figure 24, the permeate water flux increased from 6.44 kg/m^{2}h to 18.87 kg/m^{2}h with an increase in feed temperature from 50°C to 80°C. These results can be explained by Figure 25, in that increased temperature difference across the membrane helps increase vapor pressure on the feed side.

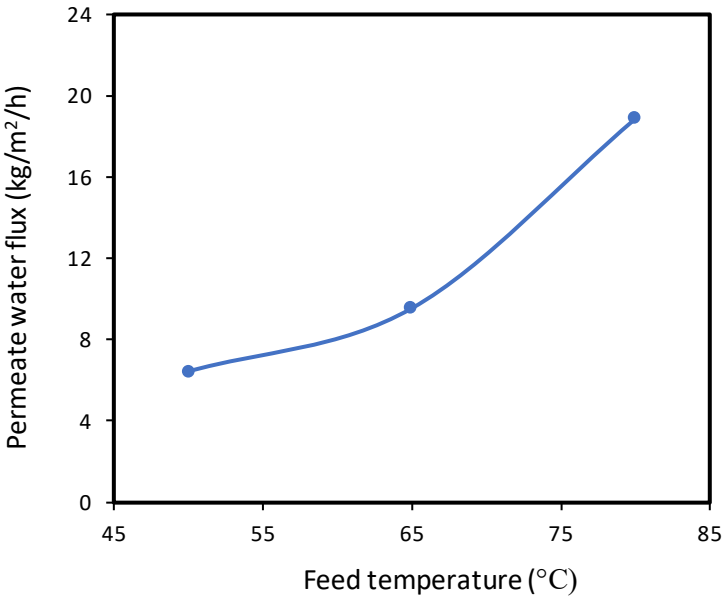

Figure 24. Effect of feed temperature on permeate water flux of the J-HFM DCMD process

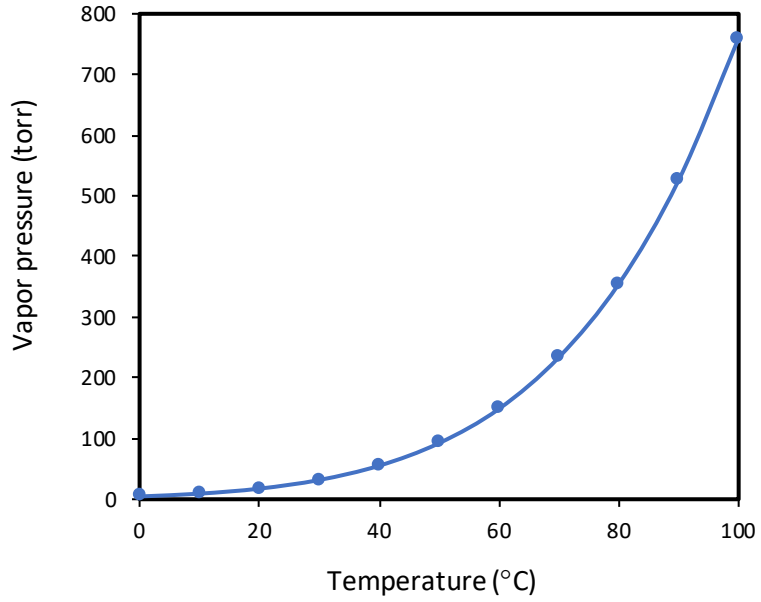

Figure 25. Effect of feed temperature on water vapor pressure (Ambrose and Lawrenson 1972)

3.4.4 Effect of Flow Velocity on Permeate Water Flux

The feed velocity effect on the water recovery during the J-HFM DCMD process is shown in Figure 26. For this assessment, flow velocities were 0.05 m/s, 0.15 m/s, and 0.3 m/s for the hot feed solution; flow velocities were 1.0 m/s, 1.5 m/s, and 3.0 m/s for the cold permeate water. The

flow velocities were selected based on the flow capacity of the circulation pumps available in the laboratory. It was found that water recovery increased linearly with operating time at different flow velocities. Table 4 lists permeate water flux values, which indicate that higher permeate water flux was obtained at higher flow velocities. For instance, at a fixed permeate velocity, the water flux increased sharply from 15.94 kg/m^{2}h to 41.04 kg/m^{2}h when the feed velocity increased from 0.05 m/s to 0.15 m/s. The flux then slightly increased to 48.10 kg/m^{2}h when the feed velocity was further raised to 0.30 m/s. Similarly, at a fixed feed velocity, the permeate water flux increased from 23.2 kg/m^{2}h to 44.53 kg/m^{2}h when the cold permeate velocity increased from 0.5 m/s to 3.0 m/s. This phenomenon can be explained by the presence of a thermal boundary layer between the hot feed side and the cold permeate side. At low flux rates, low water flux was observed due to the formation of a relatively thick thermal boundary layer (Manawi et al. 2014). As feed velocity increased, the thermal boundary layer became thinner and the heat transfer coefficient increased; this eventually reduced both temperature and concentration polarization effects and resulted in increased permeate water flux (Lokare et al. 2017).

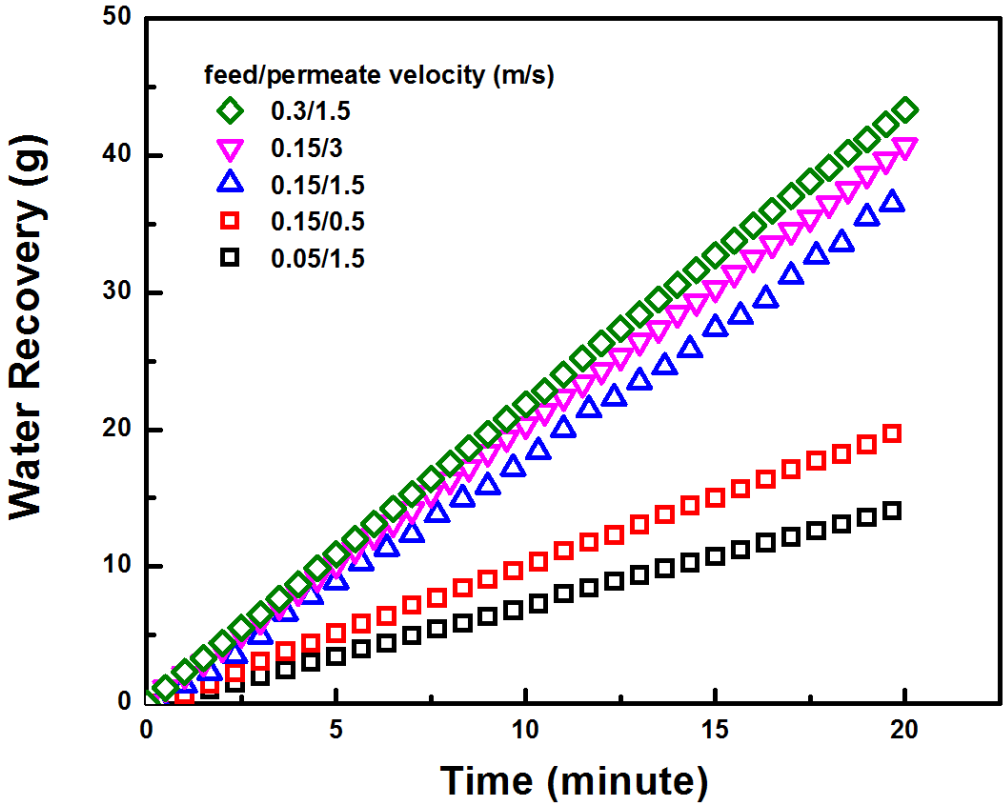

Figure 26. Water recovery at different feed velocities during the J-HFM DCMD process

Table 4. Permeate water flux at different flow velocities

Feed Velocity (m/s)	Water Flux (kg/m^{2}h), Cold Permeate Side		
NA (hot feed side)	0.5	1.5	3
0.05	--	15.94	--
0.15	23.2	41.04	44.53
0.3	--	48.10	--

Note – Temperature T_f= 80 °C, T_p=20 °C

3.4.5 Effect of Flow Velocity on Energy Efficiency

Table 5 shows temperature profiles during the DCMD experiments at different feed and permeate velocities. The hollow fiber membrane module was assembled by sealing 10 hollow fibers in stainless steel tubing; the lumen side diameters of the hollow fiber membrane and the tubing were 300 µm and 6.35 mm, respectively. The linear flow velocity of the cold permeate solution in the lumen side of the hollow fibers was changed from 0.5 m/s to 3 m/s, with the correlated range of volumetric flow rates being 21.6 ml/min to 129.6 ml/min. The velocity of the hot feed saline water in the shell side varied from 0.05 m/s to 0.3 m/s, with the correlated volumetric flow rate ranging from 40.5 ml/min to 245.7 ml/min, respectively.

The data in Table 5 show that when the permeate water velocity was fixed at 1.5 m/s, the outlet temperatures of both permeate water and the feed solution increased with increased the hot feed velocity. This can be explained by the fact that higher feed velocity reduced the thickness of the thermal boundary layer between the hot feed side and the cold permeate side, which promoted heat transfer along the membrane and thus increased the permeate temperature. Similarly, because the velocity of the cold permeate water was constant, the outlet temperatures of both feed and permeate water decreased when the permeate flow velocity increased from 0.5 m/s to 3.0 m/s.

Table 5. Effect of flow rate on temperature profiles in the J-HFM process

Feed/Permeate Velocity (m/s)	Temperature (°C)			
	Permeate In	Permeate Out	Feed In	Feed Out
0.05/1.5	20	37.3	79.9	50.8
0.15/1.5	20	49.1	80	64.8
0.3/1.5	20	51.6	79.9	68.4
0.15/0.5	20	62.9	80	70.8
0.15/3	19.9	38.3	80	62.1

Note – Temperature: T_f= 80 °C, T_p=20 °C

Figure 27 depicts the relationship between energy efficiency and feed velocity. The upper plot in Figure 27 shows that energy efficiency increased from 36.4 percent to 59.8 percent when the hot feed velocity increased from 0.05 m/s to 0.15 m/s; energy efficiency then dropped to 46.3 percent for a feed velocity of 0.3 m/s. As previously discussed, the improved energy efficiency may be attributed to the reduced thickness of the boundary layer, which also enhanced the water flux from 15.94 kg/m^{2}h to 41.04 kg/m^{2}h. After the thickness of the boundary layer decreased to a critical point, the increased velocity resulted in declined energy efficiency.

The lower plot in Figure 27 shows energy efficiency at a constant hot feed velocity. As the permeate velocity increased from 0.5 m/s to 3.0 m/s, energy efficiency slightly increased from 55.9 percent to 59.8 percent and then decreased to 55.1 percent. Thus, compared to the hot feed velocity, the cold permeate velocity influence on energy efficiency is less significant.

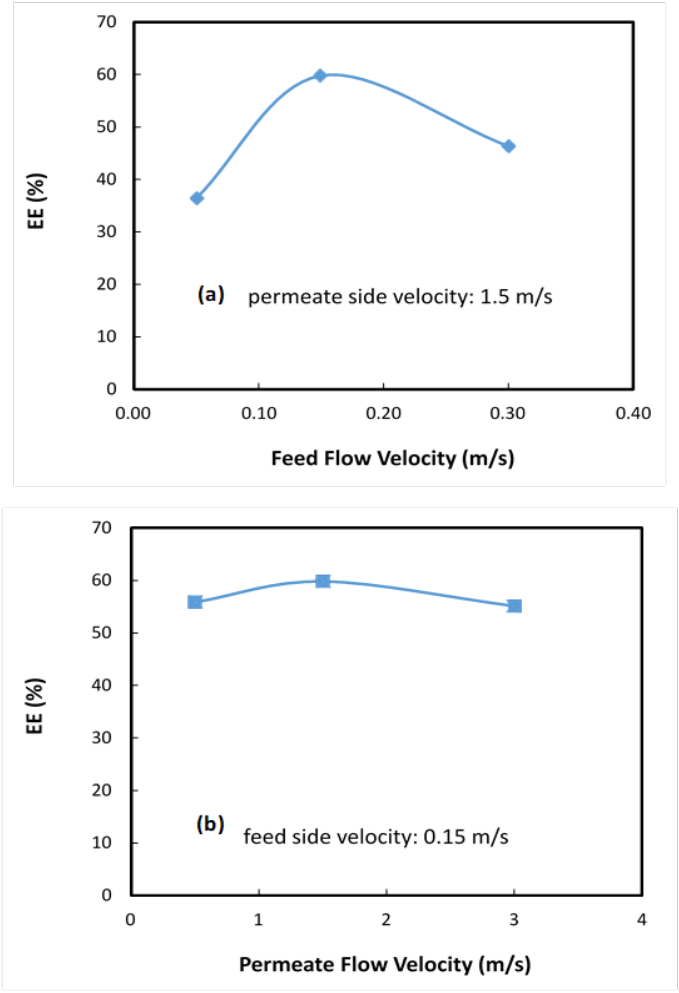

Figure 27. Energy efficiency of the J-HFM DCMD process at varied flow velocities

3.4.6 Effect of Flow Mode on Permeate Water Flux and Energy Efficiency

Figure 28 shows the mass change of cold permeate water during the J-HFM DCMD process with both co-current and counter-current flow modes. The experimental results showed that the counter-current flow arrangement produced more permeate water than the co-current flow mode at temperatures ranging from 50°C to 80°C. The permeate water flux increased with feed temperature for both the co-current and counter-current flow modes.

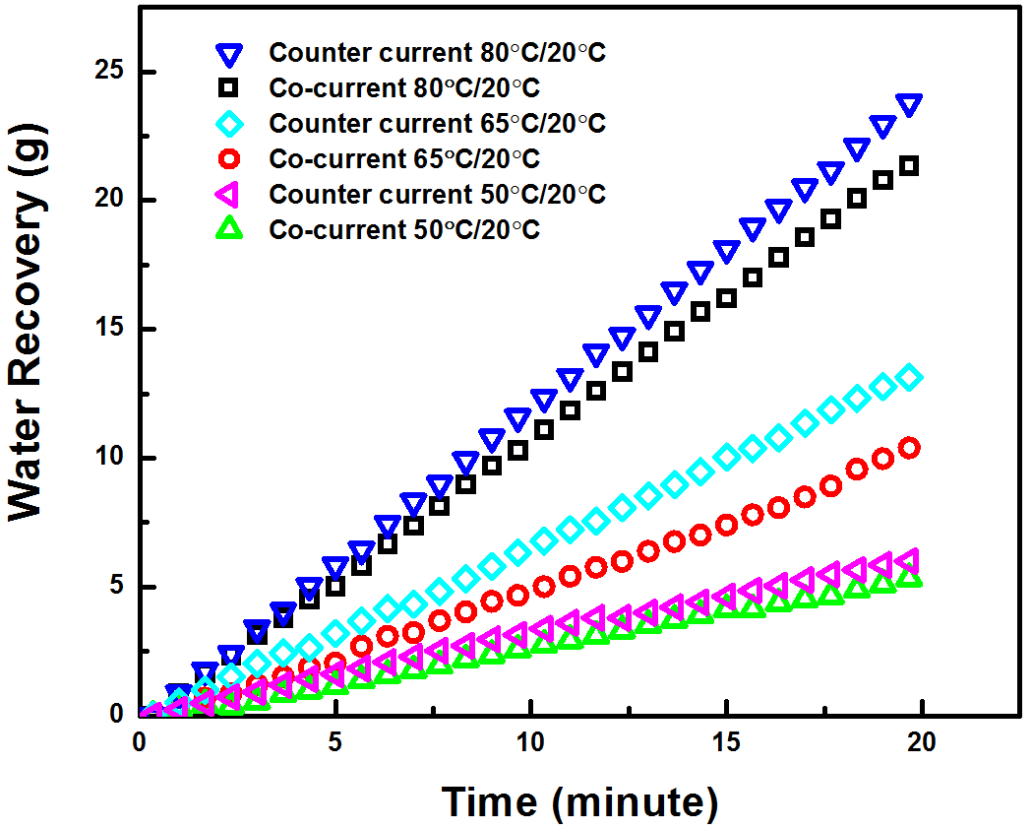

Figure 28. Water recovery during the Janus HFM DCMD process with both co-current and counter-current flow modes

Table 6 presents data for the desalination performance of the J-HFM DCMD process at different flow modes, in terms of temperature profiles, permeate water flux, and salt rejection. The data show that salt rejection results for all the desalination experiments are higher than 99.9 percent and that salt rejection was not affected by the flow arrangement.

Table 6. Desalination performance of the J-HFM DCMD process for different flow modes

Flow Mode	Temperature (°C)				Flux (kg/m^2h)	Rejection (%)
	Permeate In	Permeate Out	Feed In	Feed Out		
Co-Current	20	60.8	80	70	24.3	>99.9
		46.7	65	59.6	11.65	
		41.5	50	46.1	5.70	
Counter-Current	20	69.1	80	72.5	26.86	>99.9
		54.8	65	56.4	14.83	
		42.9	50	44	6.3	

Note – Temperature: T_f= 80 °C, T_p=20 °C; feed and permeate velocity = 0.15 m/s and 0.5 m/s

Figure 29 presents results for permeate water flux and energy efficiency of the DCMD process. The upper plot in Figure 29 clearly shows that the permeate water flux of the counter-current flow is higher than that of the co-current flow. When the feed temperature increased from 65°C to 80°C, the water flux increased from 11.65 kg/m^2h to 24.30 kg/m^2h for the co-current flow mode and from 14.83 kg/m^2h to 26.86 kg/m^2h for the counter-current flow mode. The higher permeate water flux of the counter-current flow can be attributed to the enhancement of the difference in temperature and its associated driving force.

The energy efficiency of the J-HFM DCMD desalination process is shown in the lower plot of Figure 29. With increased feed temperature from 50°C to 80°C, the energy efficiency improved from 35 percent to 53 percent for the co-current flow mode and from 23 percent to 79 percent for the counter-current flow mode. It is interesting to notice that the counter-current flow was more energy-efficient than the co-current flow at a temperature of 80°C.

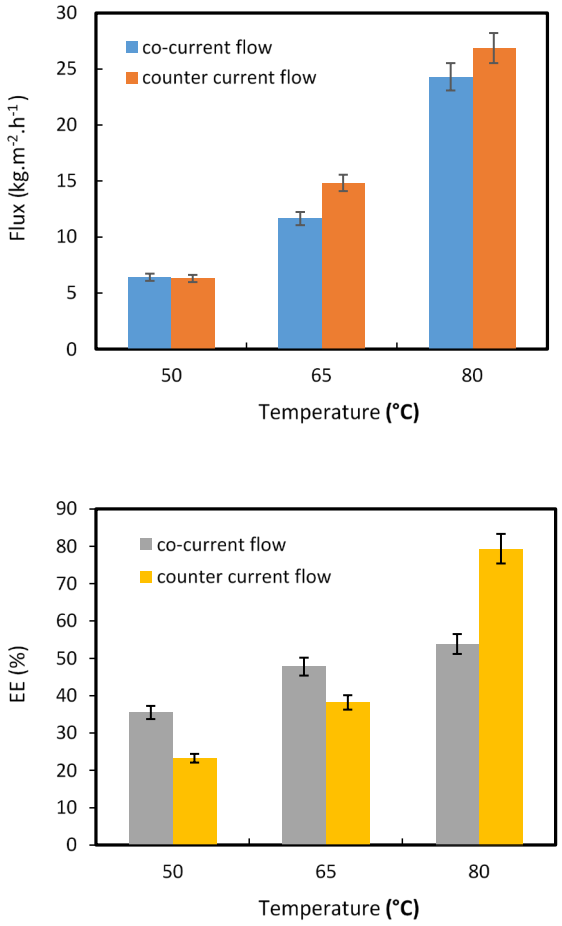

Figure 29. Permeate water flux and energy efficiency of the J-HFM DCMD process for co-current and counter-current flow modes

3.4.7 Comparison Between Neat PVDF HFM and the PVDF/PEG and PVDF/Si-R J-HFM

The desalination performance of both neat PVDF hollow fiber membrane and the J-HFM-based DCMD experiments were first validated by using 3.5 weight percent NaCl solution as feed solution; the results are shown in Figure 30. DI water was employed at the permeate side. The temperatures were 80°C and 20°C, and the flow velocities were 0.15 m/s and 0.3 m/s for the feed solution and cold permeate, respectively. The dimensions of the membrane modules were the same for the two different hollow fiber membranes; the operation condition also remained the same during the membrane distillation experiment. Therefore, the mass change on the permeate side was directly proportional to the permeate water flux. Figure 30 shows that the dual-layer J-HFM produced more water than the single-layer PVDF HFM; the corresponding permeate water flux values were 26.11 kg/m^{2}h and 22.1 kg/m^{2}h, respectively.

Figure 30 also presents salt rejection and energy efficiency results for the two different membranes. Both membranes exhibited more than 99.99 percent salt rejection, which can be attributed to the super-hydrophobicity of the PVDF membrane. The energy efficiency of the J-HFM is much higher than the neat PVDF HFM, which contributed to the presence of a porous hydrophilic inner layer on the J-HFM.

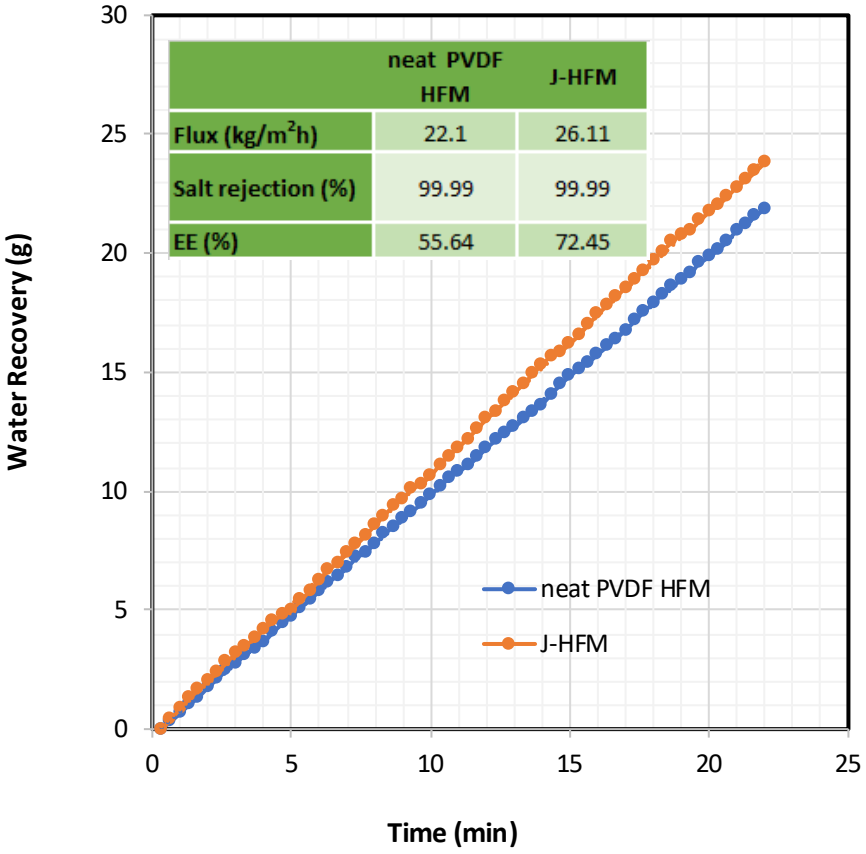

Figure 30. Comparison of desalination performance between neat PVDF HFM and the J-HFM

To investigate the stability of the J-HFM DCMD process, a continuous 82-hour experiment was performed. The temperatures of the hot feed and the cold permeate were 85.1°C and 20°C, respectively. The flow velocities of the hot feed and the cold permeate were 0.15 m/s and 0.5 m/s, respectively. Figure 31 shows the mass change of water on the cold permeate side. A mass of more than 6,066 grams of water was recovered from the feed solution with 3.5 percent NaCl. Since the feed solution was circulated during the 82 hours of operation, the feed salinity was concentrated to more than 10 percent at the end of the DCMD process.

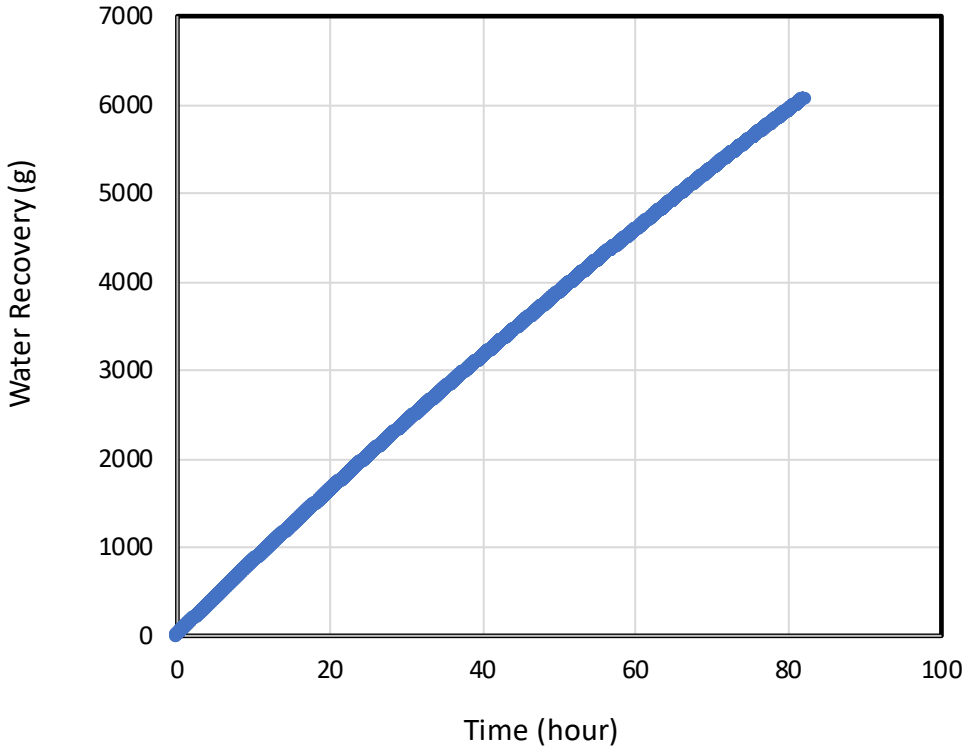

Figure 31. Permeate water recovery during a continuous 82-hour J-HFM DCMD desalination experiment

Permeate water flux and salt rejection are plotted in Figure 32. This figure shows that the water flux reduced from 33.50 kg/m^{2}h to 30.89 kg/m^{2}h in the 82 hours of continuous operation, with a water flux decline of around 7.8 percent. The water flux decline may be caused by increased feed salinity in the course of feed circulation; it can also result from membrane wetting and fouling during the long-term desalination experiment. The salt rejection remained at more than 99.9 percent in the continuous 82-hour DCMD process.

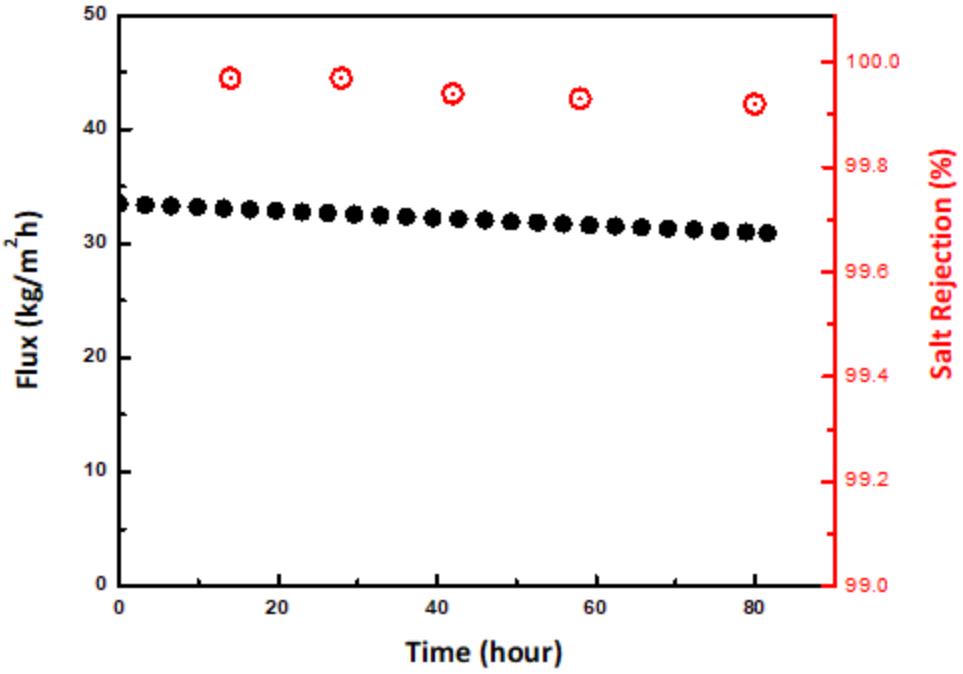

Figure 32. Desalination performance of the J-HFM in a continuous 82-hour DCMD process

3.5 Desalination of Produced Water with the J-HFM DCMD Process

3.5.1 Pretreatment and Characterization of Oilfield Produced Water

Oilfield produced water was sampled from a well production facility located at the Permian Basin in New Mexico. Figure 33 (a) shows an image of the original produced water, which shows that large amounts of dark suspended substances are present in the sample. This suspension may be attributed to oil and grease, suspended solids, dispersed oil, and various dissolved organic compounds. The salt composition and total dissolved carbon content of the produced water were characterized by ion chromatography (IC; IC-1100) and a total organic carbon analyzer (Shimadzu, TOC-L CSH). Results for total dissolved solids and total organic carbon were 154,220 mg/L and 57 mg/L, respectively.

The original produced water was pretreated with a spin-down sediment water filter to remove all suspended solids having diameters larger than 50 microns. The pretreated produced water exhibited a light yellow color as shown in Figure 33 (b). The pretreated produced water was directly used as feed solution in the J-HFM DCMD process. The permeate water from the J-HFM process is shown in Figure 33 (c).

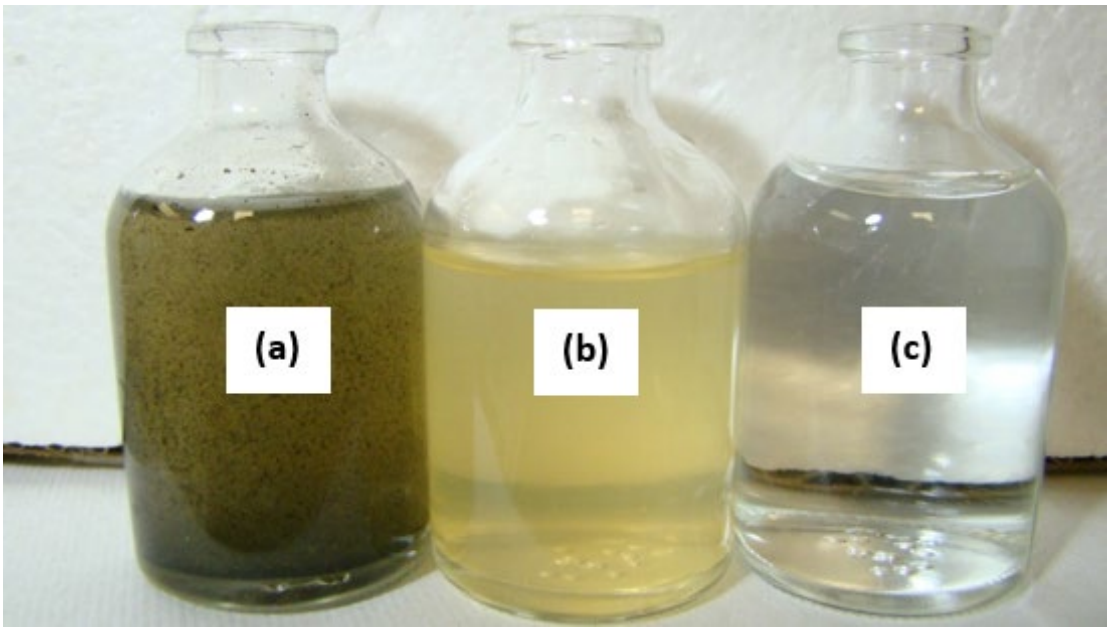

Figure 33. Image of (a) the original oilfield produced water sampled from an active production well located at Permian Basin; (b) the produced water pretreated with a 50 micron filter; and (c) the permeate water from the J-HFM DCMD process

3.5.2 Long-Term Stability of the J-HFM with Produced Water as Feed Solution

The long-term stability of the J-HFM DCMD process was assessed by using the pretreated produced water as feed solution. The produced water was circulated through the shell side of the hollow fiber membranes and distilled water flowed through the lumen side. The flow velocities of the produced water and the distilled water were 0.15 m/s (129 mL/min) and 0.5 m/s (21.6 ml/min), respectively. The temperature of the produced water was 80°C and the temperature of the distilled water at the permeate side was 20°C. During the long-term DCMD process, the mass of the permeate water was monitored by a digital balance equipped with a data acquisition system. The mass of the permeate water was recorded every 20 seconds during the 200 hours of continuous DCMD operation. The permeate water was sampled at a time interval of 8 hours to measure electrical conductivity and salt concentration.

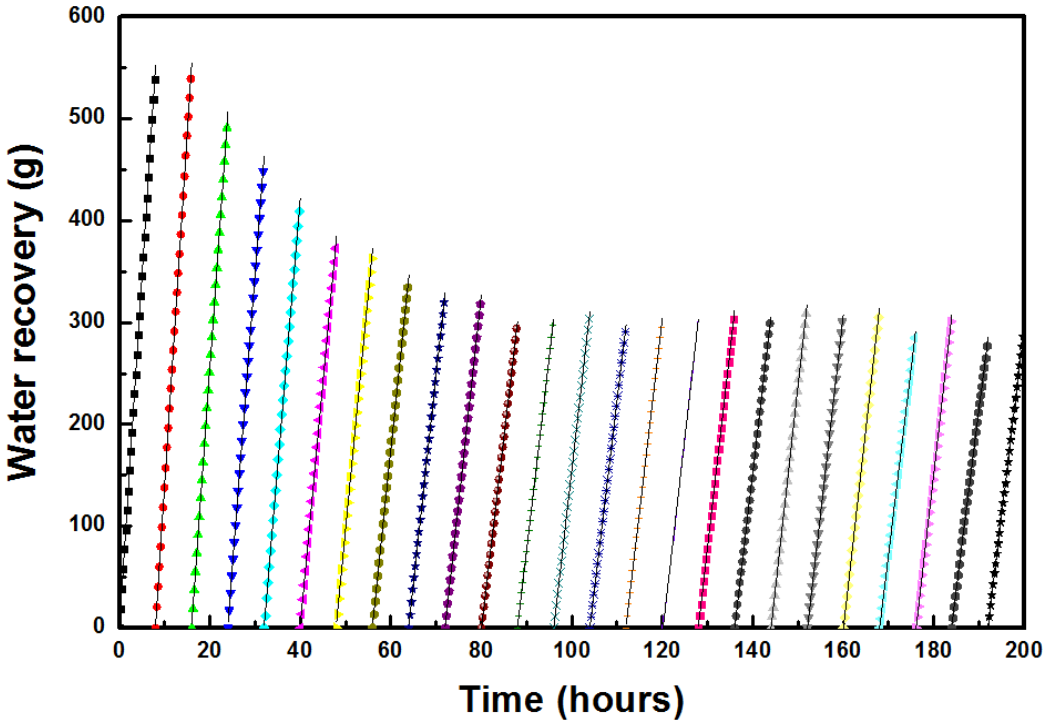

Figure 34. Mass of water recovery during a 200-hour continuous DCMD desalination process by using produced water as the feed solution

Figure 34 presents data for water recovery during the 200 hours of continuous DCMD operation. It shows that the water recovery was 552 grams for the first two 8-hours of operations, and then decreased during the time period from 16 to 24 hours. The average water recovery was 311 grams per 8 hours during the time period from 80 to 200 hours.

Figure 35 shows permeate flux and salt rejection as a function of operating time during the 200-hour continuous desalination process. As indicated by the water recovery results in Figure 34, the permeate water flux decreased from 25.41 kg/m^{2}h to 19.19 kg/m^{2}h in the first 80 hours of operation and then dropped to 15.21 kg/m^{2}h at the end of the 200 hours of operation. The salt rejection was higher than 99 percent in the first 104 hours of operation and reduced slightly to 98.2 percent at the end of the 200 hours of operation. The desalination performance decline of the membrane may be caused by water clogging; the produced water may migrate into the large pores of the PVDF/Si-R layer and result in the distilled water and the produced water making contact, thereby reducing salt rejection (Dah and Cheng 1983; Edwie and Chu8ng 2012)).

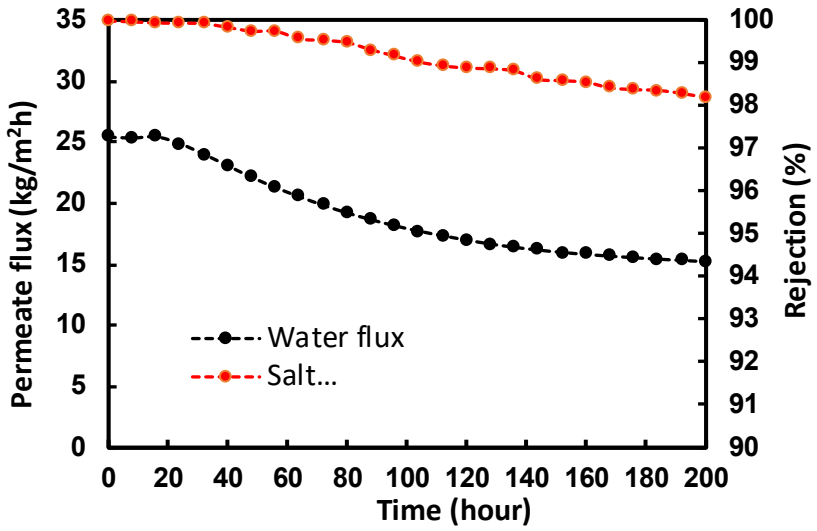

Figure 35. Water flux and salt rejection of the J-HFM DCMD desalination process during a 200-hour DCMD process with produced water as feed solution

The energy efficiency of the J-HFM DCMD desalination process is plotted in Figure 36. This figure shows that the trends of energy efficiency are consistent with the permeate water flux results shown in Figure 35, i.e., energy efficiency decreased with decreased permeate water flux. The temperature profiles of the produced water at both inlet and outlet are also plotted in Figure 36; the inlet temperature was stabilized at 80 °C and the outlet temperature slightly decreased from 64.6°C to 61.4°C. These results may be attributed to temperature polarization during the DCMD desalination process. It may also be noted that heat recovery was not considered during the DCMD process; further improvement of energy efficiency through heat recovery or process design are beyond the topic of this project.

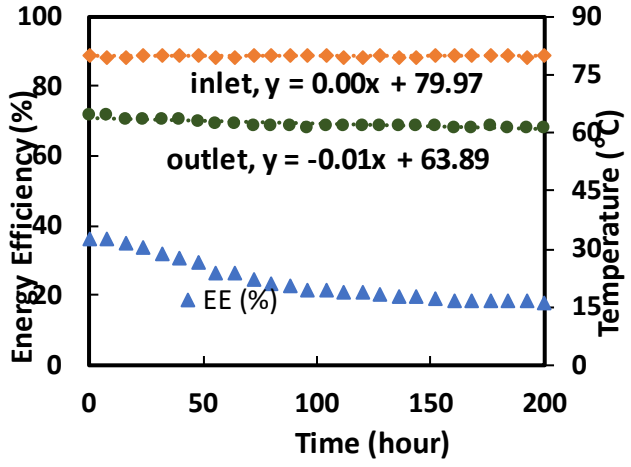

Figure 36. Energy efficiency of the J-HFM DCMD desalination process during a 200-hour DCMD process with produced water as feed solution

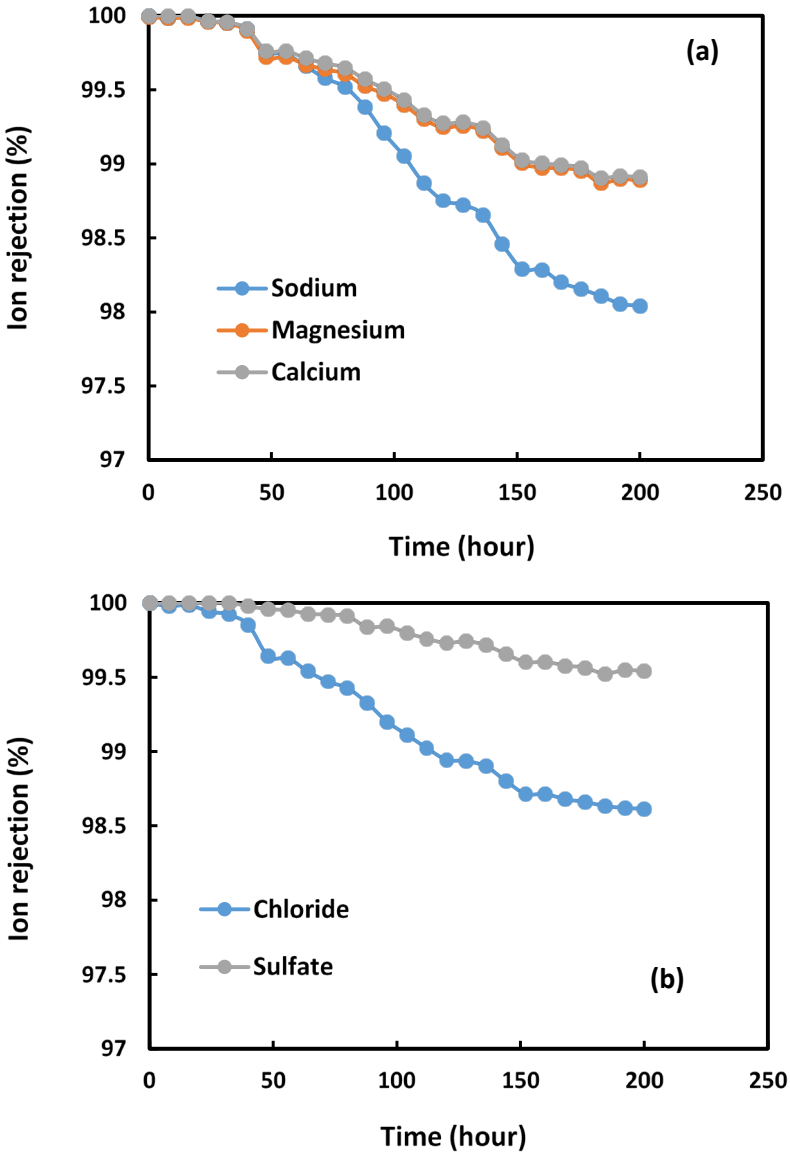

Figure 37. Rejection of the major cations and anions during the 200-hour continuous DCMD desalination process

To assess salt rejection during the 200-hour continuous DCMD desalination process, ion chromatography was used to measure ion concentrations in the permeate water. Figure 37 shows rejection efficiencies for major cations (upper plot) and anions (lower plot) present in the produced water. It shows that rejection percentages for all the ions decreased with operating time. The decreases in ion rejection efficiency may be caused by the occurrence of membrane wetting in the membrane distillation process due to using the high salinity produced water as feed solution. Once membrane pores are wet, the ions in the produced water tended to penetrate

to the permeate side due to a concentration gradient across the membrane. The rejection for the divalent ions was higher than that for the monovalent ions.

To reveal the fouling behavior of the used membrane, a field emission scanning electron microscope (FESEM) was used to examine the surface morphology of the hollow fiber membrane. Figure 38 shows the outer surface morphology of both the fresh membrane and the membrane that was used for 200 hours of continuous operation. The images show that the outer surface of the used membrane was covered by multiple layers of amorphous deposits. The composition of these deposits was further identified by energy-dispersive x-ray spectroscopy (EDX). The results show that the composition of the deposits mainly involves iron, calcium, and magnesium on the outer surface of the used membrane (Figure 39).

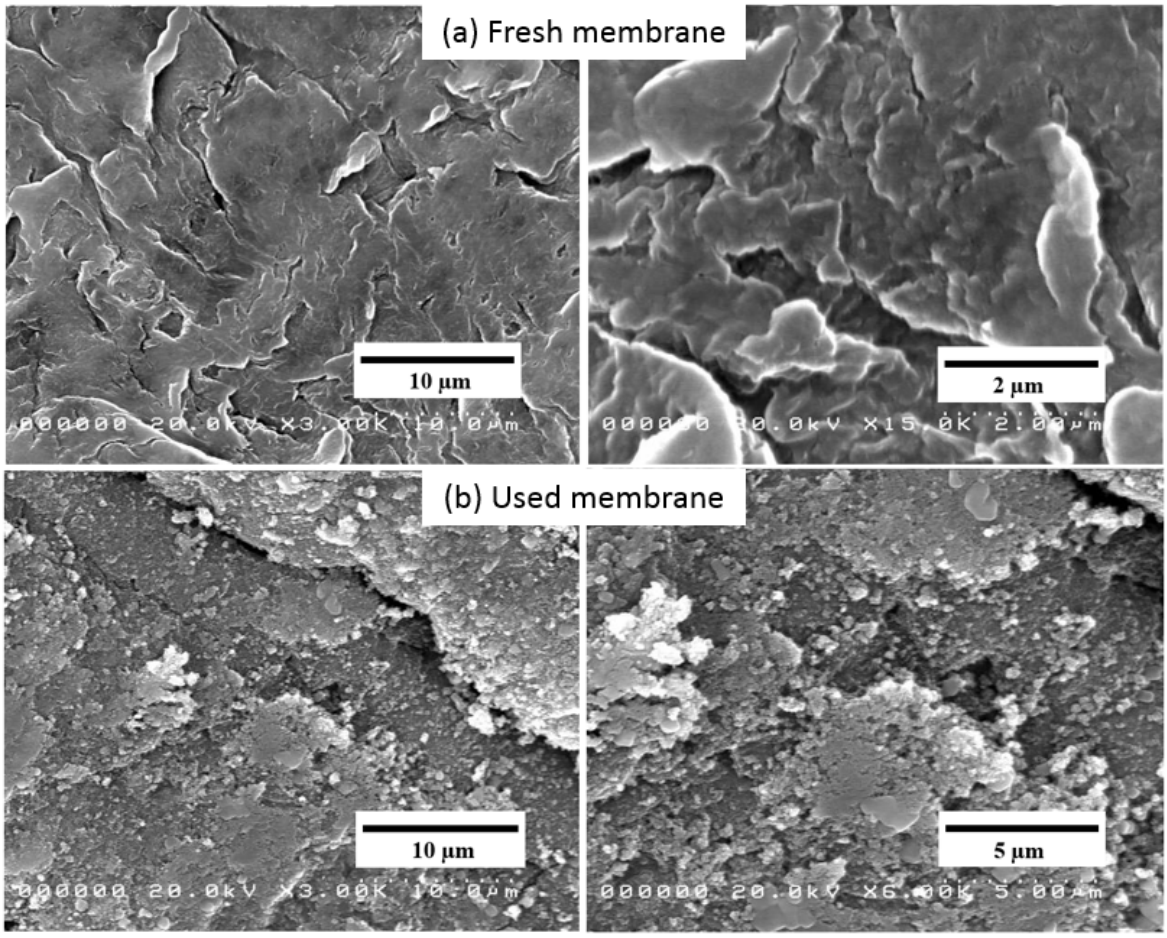

Figure 38. Outer surface morphology of (a) clean J-HFM; and (b) the membrane after 200 hours of continuous DCMD desalination operation

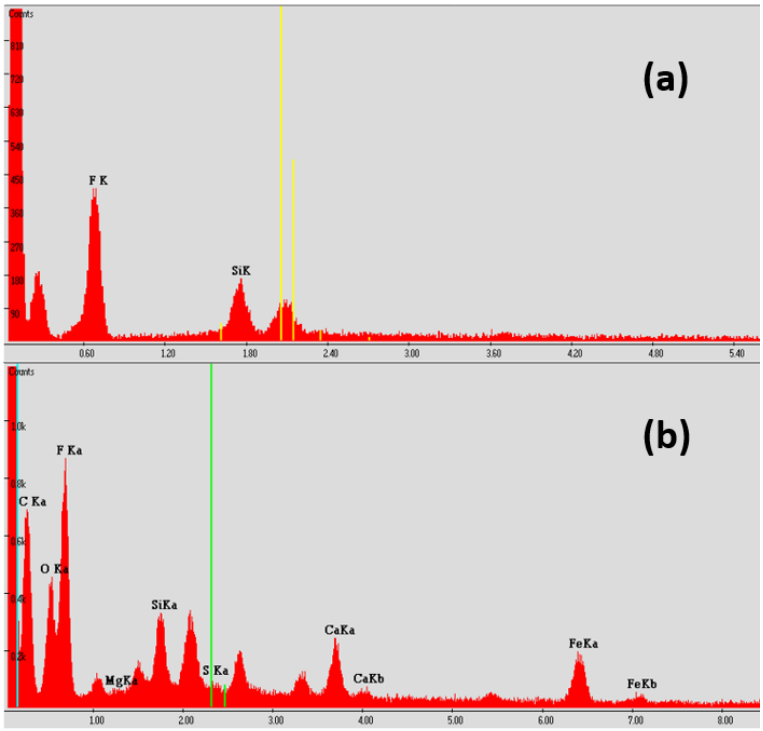

Figure 39. EDX on the outer surface of (a) fresh membrane; and (b) used membrane

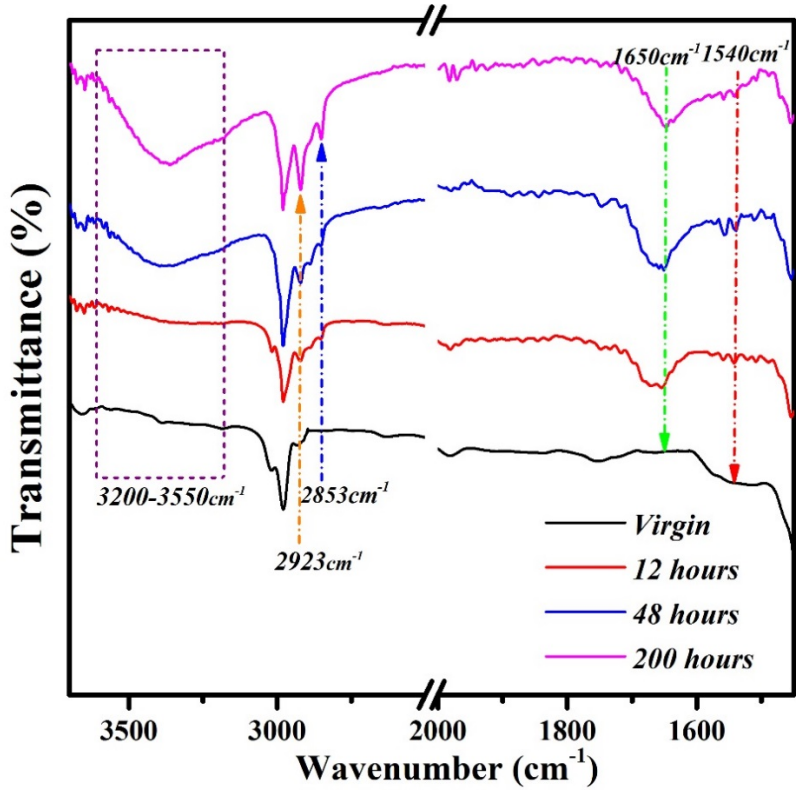

Figure 40. ATR-FTIR of (a) fresh membrane; and (b) used membrane

The presence of high content non-purgeable organic carbon (NPOC), a unique characteristic of the oilfield produced water, is a significant challenge for the membrane. At the end of the 200-hour J-HFM DCMD process, NPOC was significantly reduced from 57.6 mg/l to less than 2.0 mg/L. Attenuated total reflection-FTIR (ATR-FTIR) spectroscopy was used to examine the organic composition of the deposition on the outer surface of the used membrane. Compared to the fresh membrane, Figure 40 shows that three new peak bands were found on the outer surface of the used membrane, and that the transmittance intensity was proportional to operating time. The three peak bands (located at 1500 to 1700cm^{-1}, 2850 to 3000cm^{-1}, and 3200 to 3550 cm^{-1}) mainly originate from amide II I bands, symmetric and asymmetric starching of –CH2 groups, and the stretching of O–H groups, respectively (Du et al. 2018). These peaks are attributed to aliphatic hydrocarbons, aromatic hydrocarbons, carbonates (which represent proteins), aliphatic hydrocarbons, and humic substances that are commonly detected in oilfield produced water (Duh et al. 2018; Bell et al. 2017; Lu et al. 2017).

Figure 41 shows the inner surface morphology of the fresh membrane and the used membrane. The inner layer shows a typical bi-continuous morphology with a highly interconnected pore structure. It is interesting to note that the used membrane exhibits an extremely clean inner surface after a continuous 200 hours of desalination operation. Since the amount of the permeated salts is small in the permeate water, the distilled water at the lumen side helps flush out all the salts from the inner layer and thereby avoids the formation of salt deposits on the inner surface.

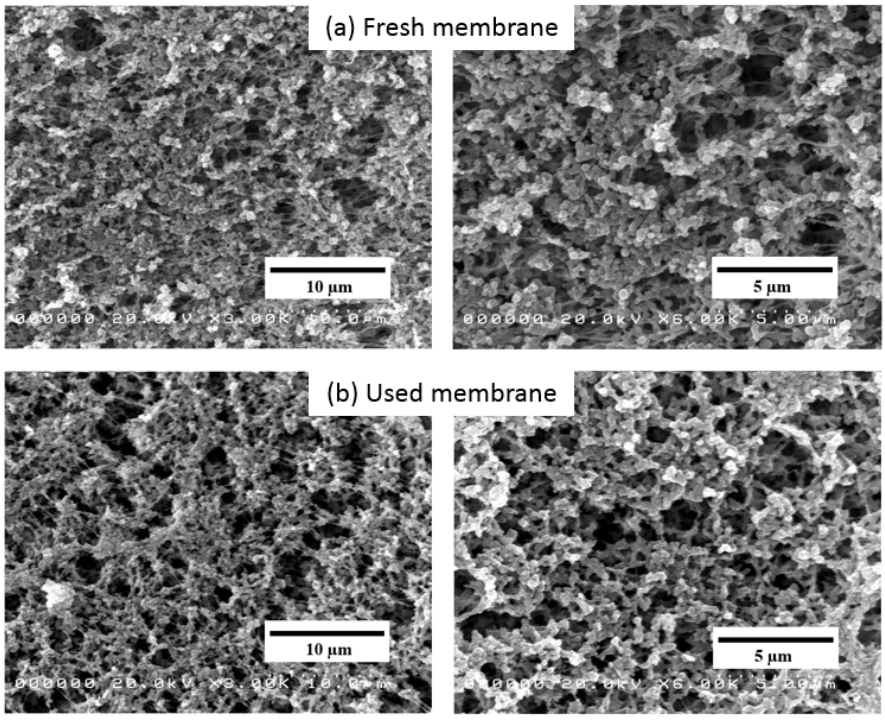

Figure 41. Inner surface morphology of (a) clean J-HFM; and (b) the membrane after 200 hours of continuous DCMD desalination operation

Liquid entry pressure (LEP) is the minimum pressure required to penetrate the liquid through the membrane. The LEPs of both the fresh membrane and the used membrane were measured by lab-made apparatus shown in Figure 42. The shell side of the hollow fiber membrane was circulated with DI water (the original conductivity less than 5 uS/cm). The lumen side of the module was connected to a pump filled with 3.5 weight percent saline water. The DI water in the shell side was circulated at a constant flow rate and the conductivity of the distilled water was monitored by a conductivity meter. During LEP measurement, the operating pressure was raised 0.01 bar every 10 minutes. Once the conductivity increased sharply, the corresponding pressure was recorded as the LEP.

Table 7 shows LEP data for the fresh membrane and for the used membrane after long-term continuous operation. The LEP decreased from 1.23 bar to 0.55 bar with 48 hours of continuous operation, and it dropped to 0.10 bar at the end of the 200 hours of continuous DCMD process. The reduced LEP indicated the occurrence of membrane wetting when using the high salinity produced water as feed solution; this occurs because salts at the feed side accelerate membrane wetting (Ge et al. 2014).

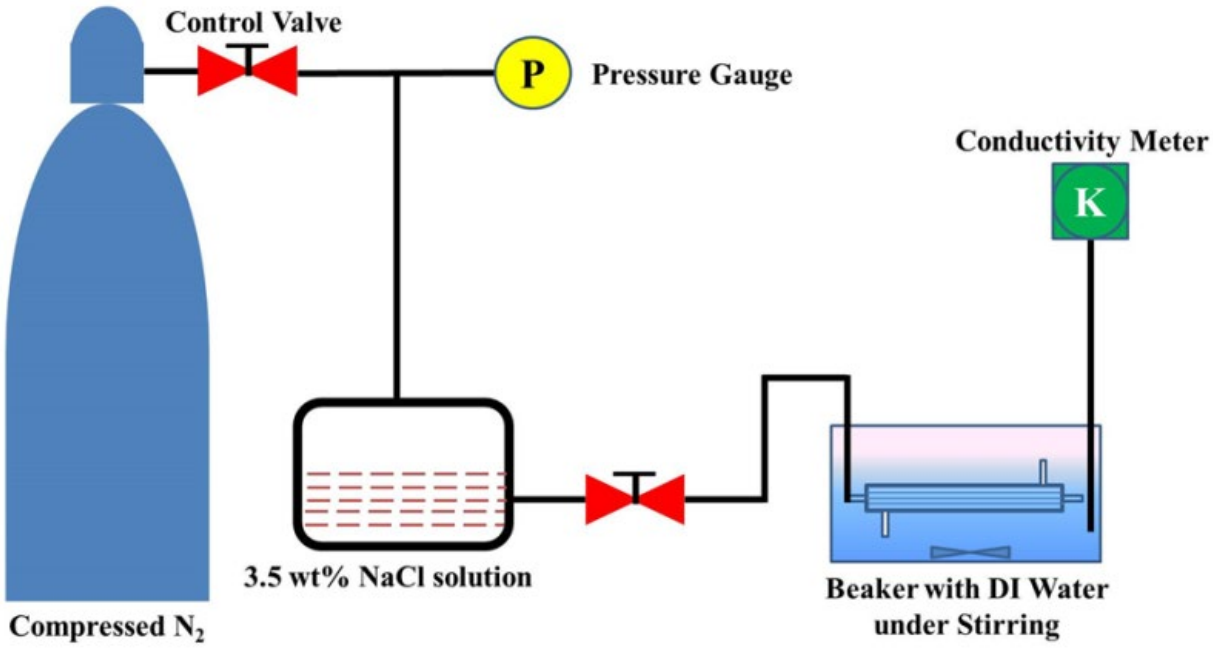

Figure 42. Lab-made apparatus for LEP measurement

Table 7. LEP Measurement of the membranes

Dope Solution Composition	LEP (bar)
Fresh membrane	1.23
Used membrane – 48 hours	0.55
Used membrane – 200 hours	0.10

3.5.3 Regeneration Effect on Water Flux and Salt Rejection

Membrane regeneration is a conventional approach to address the fouling problem in a typical DCMD desalination process. To study the membrane regeneration effect on the DCMD desalination performance, a 72-hour DCMD experiment was conducted with membrane regeneration at an interval of every12 hours. The regeneration was achieved by DI water flushing at the feed side of the membranes with a flow rate of 0.32 m/s (259.2 ml/min).

Figure 43 (a) shows the mass of water recovery during a continuous 72 hours of DCMD desalination process without membrane regeneration. The water recovery starts to decline at the end of 16 hours of operation, and it decreased further with additional operating time. The decline was 40 percent at the end of the operation, which can be explained by the accumulated salt and organic deposits on the outer surface of the membrane, intensifying both membrane wetting and scale fouling. When membrane regeneration was performed, Figure 43 (b) shows that the reduction of water recovery is small at the end of the 72 hours of operation. Figure 44 plots both permeate water flux and salt rejection of the J-HFM in the 72-hour operation with membrane regeneration. The permeate flux decreased from 24.3 kg/m^{2}h to 21.64 kg/m^{2}h, and the flux decline was 9.4 percent, which shows a significant permeate flux improvement compared to the membrane without generation. The salt rejection was more than 99.4 percent at the end of the 72-hour desalination process.

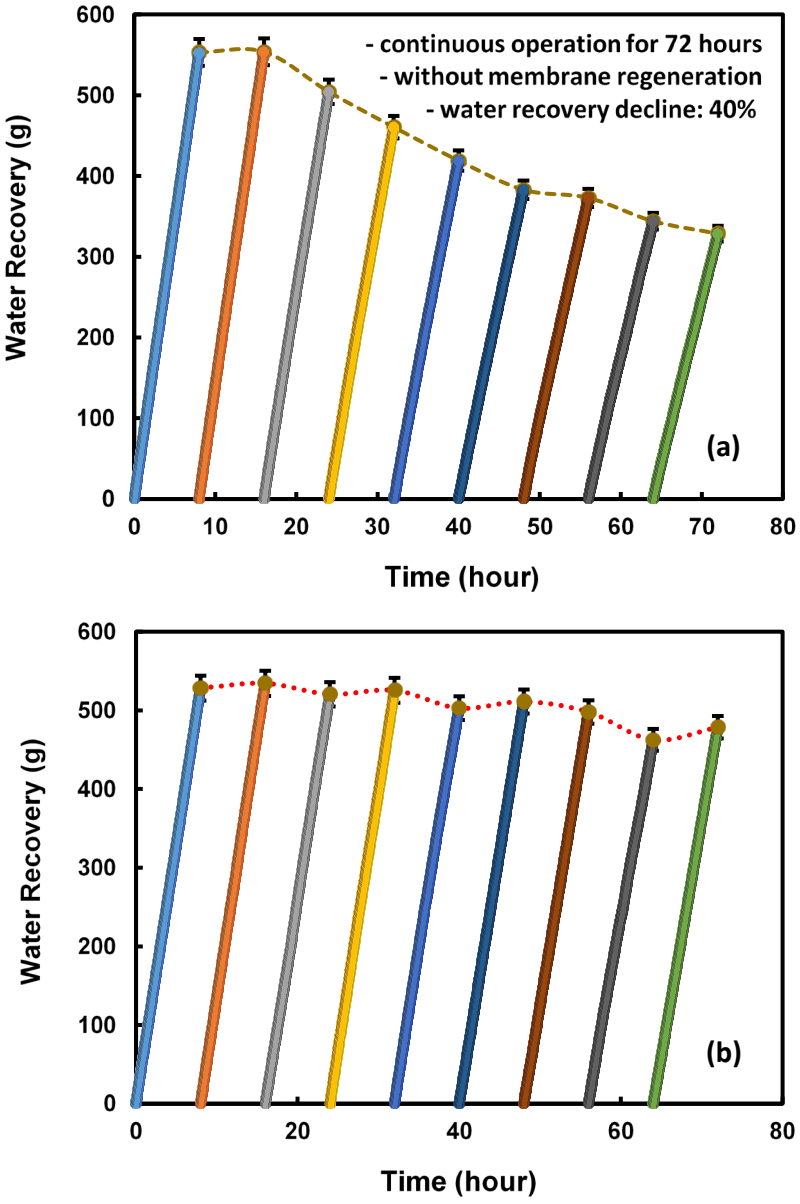

Figure 43. Mass of water recovery during a 72-hour continuous DCMD desalination process (a) without membrane regeneration process; and (b) with membrane regeneration process

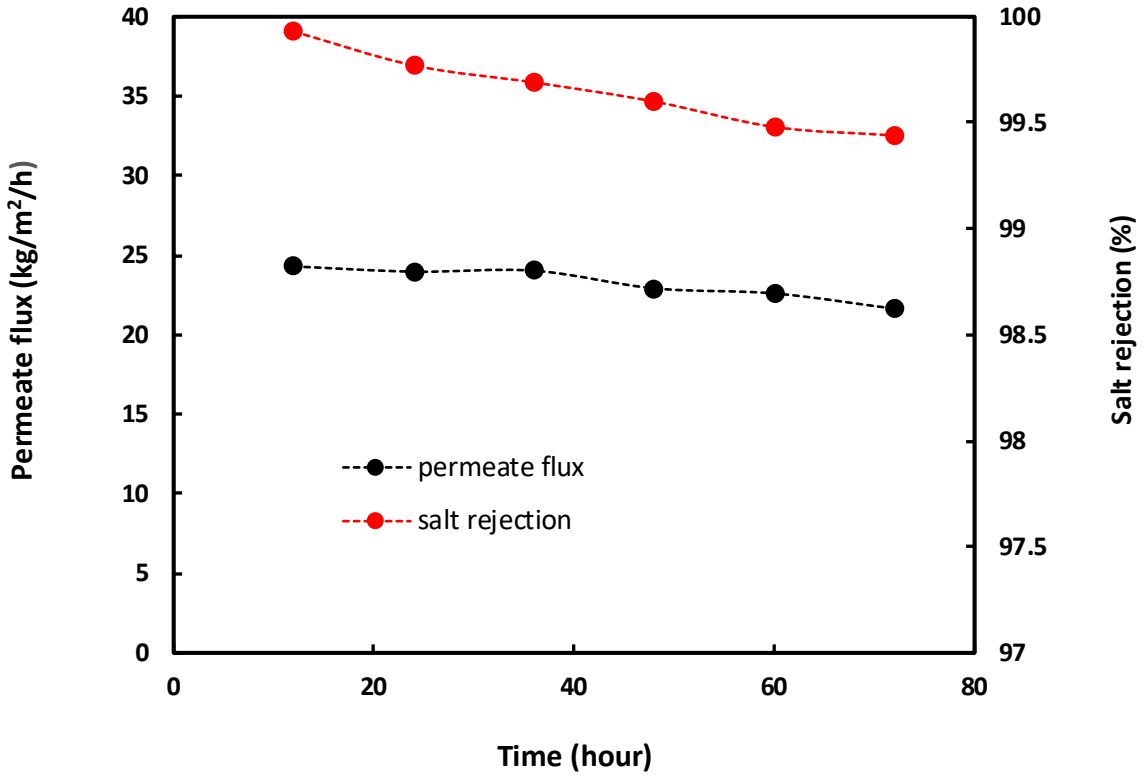

Figure 44. Permeate flux and salt rejection of the J-HFM DCMD desalination process during a 72-hour DCMD process with membrane regeneration

Figure 45 shows permeate flux and salt rejection results for the DCMD process with use of the permeate water for membrane regeneration. This scenario is more realistic due to the fact that DI water is usually not available in the field. Based on an average salt rejection efficiency of 99.9 percent in the first 24 hours of operation, the TDS of the permeate water was 150 ppm. Figure 45 shows that the salt rejection of the J-HFM remains more than 99.8 percent after the 72 hours of continuous DCMD operation. Compared to the results shown in Figure 43, the decline of permeate water flux was more significantly reduced, from 40 percent to 10 percent; this is comparable with the results in Figure 44. It can be concluded that the permeate water from the DCMD process can be used to regenerate the J-HFM, which can help reduce the demand for fresh water in the desalination process.

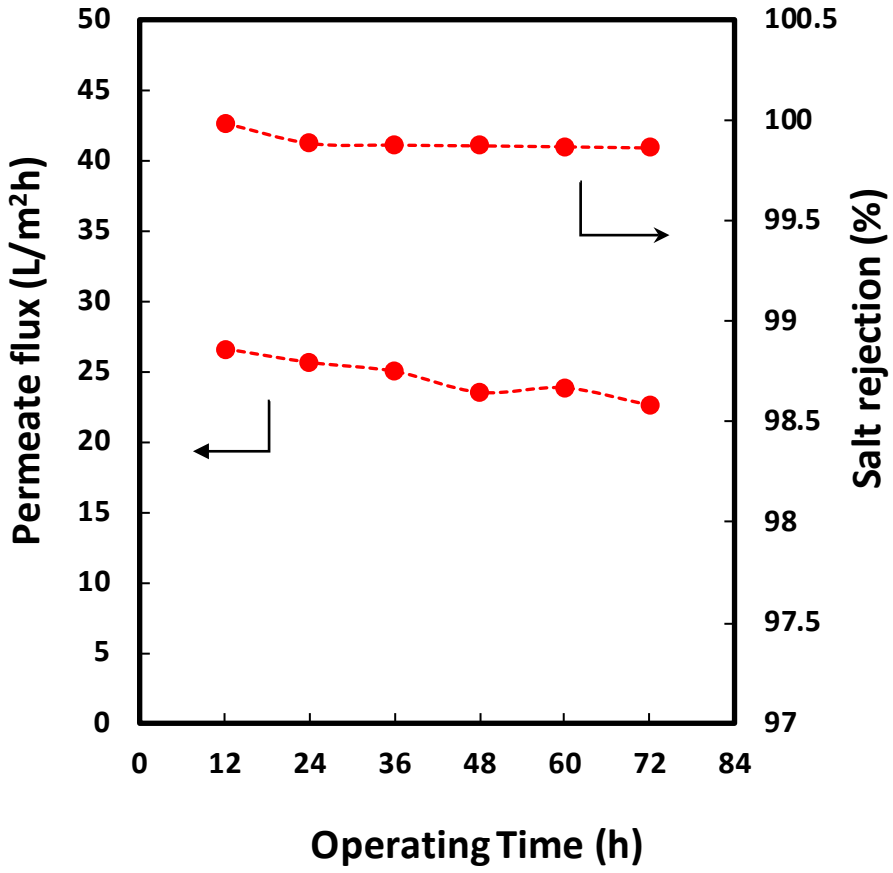

Figure 45. Permeate flux and salt rejection of the J-HFM DCMD desalination process during a 72-hour DCMD process with membrane regeneration

4 Conclusion

In this study, two different J-HFMs were prepared with the same hydrophobic PVDF/Si-R outer layer and different hydrophilic inner layers of PES/PEG and PVDF/PEG. The PVDF/PEG and PVDF/Si-R J-HFMs were chosen for DCMD desalination due to their larger pore size and interconnected microstructures. The operation parameter effects on the J-HFM DCMD, including feed salinity, flow velocity, and flow mode, were investigated in terms of permeate water flux, salt rejection, and energy efficiency. Compared to neat PVDF hollow fiber membrane, the J-HFM exhibited both increased permeate water flux and improved energy efficiency in the DCMD process. The permeate water flux decline was 7.8 percent in a continuous 82-hour desalination experiment. The salt rejection remained at more than 99.9 percent during the DCMD process. Oilfield produced water was sampled for a 200-hour continuous DCMD experiment. The results show that the permeate water flux declined from 25.41 kg/m^{2}h to 15.21 kg/m^{2}h, and that salt rejection was 98.4 percent at the end of the 200 hours of operation. The

results of SEM and FTIR confirmed that multiple layers of deposits accumulated at the feed side of the membrane, including scales and dissolved organics from the produced water. Membrane regeneration was achieved by using both DI water and the permeate solution in the DCMD process; the results show significantly improved permeate water flux.

This page intentionally left blank.

References

Citation in Text	Reference
Al-Obaidani et al. 2008	Al-Obaidani, S., E. Curcio, F. Macedonio, G. Di Profio, H. Al-Hinai, and E. Drioli. 2008. "Potential of Membrane Distillation in Seawater Desalination: Thermal Efficiency, Sensitivity Study and Cost Estimation." *Journal of Membrane Science* 323, pp. 85-98.
Ambrose and Lawrenson 1972	Ambrose D. and I. J. Lawrenson. 1972. "The vapor pressure of water". *The Journal of Chemical Thermodynamics* 4, pp: 755-761.
Bell et al. 2017	Bell, E. A., T. E. Poynor, K. B. Newhart, J. Regnery, B. D. Coday, and T. Y. Cath. 2017. "Produced Water Treatment using Forward Osmosis Membranes: Evaluation of Extended-Time Performance and Fouling." *Journal of Membrane Science* 525, pp. 77-88.
Bonyadi and Chung 2007	Bonyadi, S. and T. S. Chung. 2007. "Flux Enhancement in Membrane Distillation by Fabrication of Dual Layer Hydrophilic–Hydrophobic Hollow Fiber Membranes." *Journal of Membrane Science* 306, pp. 134-146.
Dah and Cheng 1983	Dah, S. J. W. and Y. Cheng. 1983. "Composite Membrane for a Membrane Distillation System." U.S. Patent 4,419,242.
Du et al. 2018	Du, X., Z. Zhang, K. H. Carlson, J. Lee, and T. Tong. "Membrane Fouling and Reusability in Membrane Distillation of Shale Oil and Gas Produced Water: Effects of Membrane Surface Wettability." *Journal of Membrane Science* 567, pp. 199-208.
Edwie and Chung 2012	Edwie, F. and T. S. Chung. 2012. "Development of Hollow Fiber Membranes for Water and Salt Recovery from Highly Concentrated Brine via Direct Contact Membrane Distillation and Crystallization." *Journal of Membrane Science* 421-422, pp. 111-123.
Elsayed et al. 2015	Elsayed, N. A., M. A. Barrufet, and M. M. El-Halwagi. 2015. "An Integrated Approach for Incorporating Thermal Membrane Distillation in Treating Water in Heavy Oil Recovery using SAGD." *Journal of Unconventional Oil and Gas Resources* 12, pp. 6-14.
Ge et al. 2014	Ge, J., Y. Peng, Z. Li, P. Chen, and S. Wang. 2014. "Membrane Fouling and Wetting in a DCMD Process for RO Brine Concentration." *Desalination* 344, pp. 97-107.
Guendouzi et al. 2001	Guendouzi, M. E., A. Dinane, and A. Mounir. 2001. "Water Activities, Osmotic and Activity Coefficients in Aqueous Chloride Solutions at T= 298.15 K by the Hygrometric Method." *The Journal of Chemical Thermodynamics* 33, pp. 1059-1072.
Hickenbottom and Cath 2014	Hickenbottom, K. L. and T. Y. Cath. 2014. "Sustainable Operation of Membrane Distillation for Enhancement of Mineral Recovery from Hypersaline Solutions." *Journal of Membrane Science* 454, pp. 426-435.

Citation in Text	Reference
Khayet et al. 2005	Khayet, M., J. I. Mengual, and T. Matsuura. 2005. "Porous Hydrophobic/Hydrophilic Composite Membranes: Application in Desalination using Direct Contact Membrane Distillation." *Journal of Membrane Science* 252, pp. 101-113.
Khayet et al. 2006	Khayet, M., T. Matsuura, J. I. Mengual, and M. Qtaishat. 2006. "Design of Novel Direct Contact Membrane Distillation Membrane." *Desalination* 192, pp. 105-111.
Li et al. 2017	Li, L., L. Song, and K. K. Sirkar. 2017. "Desalination Performances of Large Hollow Fiber-Based DCMD Devices." *Industrial & Engineering Chemistry Research* 56, pp. 1594-1603.
Lokare et al. 2017	Lokare, O. R., S. Tavakkoli, S. Wadekar, V. Khanna, and R. D. Vidic. 2017. "Fouling in Direct Contact Membrane Distillation of Produced Water from Unconventional Gas Extraction." *Journal of Membrane Science* 524, pp. 493-501.
Lu et al. 2017	Lu, X., Y. Peng, H. Qiu, X. Liu, and L. Ge. 2017. "Anti-Fouling Membranes by Manipulating Surface Wettability and their Anti-Fouling Mechanism." *Desalination* 413, pp. 127-135.
Macedonio et al. 2014	Macedonio, F., A. Ali, T. Poerio, E. El-Sayed, E. Drioli, and M. Abdel-Jawad. 2014. "Direct Contact Membrane Distillation for Treatment of Oilfield Produced Water." *Separation and Purification Technology* 126, pp. 69-81.
Manawi et al. 2014	Manawi, Y. M., M. Khraisheh, A. K. Fard, F. Benyahia, and S. Adham. 2014. "Effect of Operational Parameters on Distillate Flux in Direct Contact Membrane Distillation (DCMD): Comparison between Experimental and Model Predicted Performance." *Desalination* 336, pp. 110-120.
Minier-Matar et al. 2014	Minier-Matar, J., A. Hussain, A. Janson, and S. Adham. 2014. "Treatment of Produced Water from Unconventional Resources by Membrane Distillation." Proceedings from the *International Petroleum Technology Conference*. Doha, Qatar, January 2014.
Phattaranawik et al. 2003	Phattaranawik, J., R. Jiraratananon, and A. G. Fane. 2003. "Effect of Pore Size Distribution and Air Flux on Mass Transport in Direct Contact Membrane Distillation." *Journal of Membrane Science* 215, pp. 75-85.
Qtaishat et al. 2008	Qtaishat, M., T. Matsuura, B. Kruczek, and M. Khayet. 2008. "Heat and Mass Transfer Analysis in Direct Contact Membrane Distillation." *Desalination* 219, pp. 272-292.
Singh and Sirkar 2012	Singh, D. and K. K. Sirkar. 2012. "Desalination of Brine and Produced Water by Direct Contact Membrane Distillation at High Temperatures and Pressures." *Journal of Membrane Science* 389, pp. 380-388.
Singh et al. 2013	Singh, D., P. Prakash, and K.K. Sirkar. 2013. "Deoiled Produced Water Treatment Using Direct-Contact Membrane Distillation." *Industrial & Engineering Chemistry Research* 52, pp. 13439-13448.

Citation in Text	Reference
Ullah et al. 2018	Ullah, R., M. Khraisheh, R. J. Esteves, J. T. McLeskey, M. AlGhouti, M. Gad-el-Hak, and H. Vahedi Tafreshi. 2018. "Energy Efficiency of Direct Contact Membrane Distillation." *Desalination* 433, pp. 56-67.
Wang et al. 2017	Wang L. Y., W. F. Yong, L. E. Yu, T. S. Chung. 2017. "Design of high efficiency PVDF-PEG hollow fibers for air filtration of ultrafine particles." *Journal of Membrane Science* 535, pp. 342-349.
Zhang et al. 2010	Zhang, J., N. Dow, M. Duke, E. Ostarcevic, J. D. Li, and S. Gray. 2010. "Identification of Material and Physical Features of Membrane Distillation Membranes for High Performance Desalination." *Journal of Membrane Science* 349, pp. 295-303.
Zhu et al. 2015	Zhu, J., L. Jiang, and T. Matsuura. 2015. "New Insights into Fabrication of Hydrophobic/Hydrophilic Composite Hollow Fibers for Direct Contact Membrane Distillation." *Chemical Engineering Science* 137, pp. 79-90.